Identification and quantification of chemical reactions in a coastal aquifer to assess submarine groundwater discharge composition

Tybaud Goyetche, Linda Luquot, Jesus Carrera, Laura Martínez-Pérez, Albert Folch

▶ **To cite this version:**

Tybaud Goyetche, Linda Luquot, Jesus Carrera, Laura Martínez-Pérez, Albert Folch. Identification and quantification of chemical reactions in a coastal aquifer to assess submarine groundwater discharge composition. Science of the Total Environment, 2022, 838 (1), pp.155978. 10.1016/j.scitotenv.2022.155978 . hal-03796089

HAL Id: hal-03796089
https://hal.umontpellier.fr/hal-03796089v1

Submitted on 17 Oct 2022

HAL is a multi-disciplinary open access archive for the deposit and dissemination of scientific research documents, whether they are published or not. The documents may come from teaching and research institutions in France or abroad, or from public or private research centers.

L'archive ouverte pluridisciplinaire **HAL**, est destinée au dépôt et à la diffusion de documents scientifiques de niveau recherche, publiés ou non, émanant des établissements d'enseignement et de recherche français ou étrangers, des laboratoires publics ou privés.

Title: Identification and quantification of chemical reactions in a coastal aquifer to assess submarine groundwater discharge composition

Tybaud Goyetche[1,2,3*], Linda Luquot[4], Jesus Carrera[1,2], Laura Martínez Pérez[1,2,3], Albert Folch[2,3]

[1] Institute of Environmental Assessment and Water Research (IDAEA), CSIC, Jordi Girona 18, 08034 Barcelona, Spain

[2] Associated Unit: Hydrogeology group (UPC-CSIC)

[3] Department of Civil and Environment Engineering, Universitat Politècnica de Catalunya (UPC), Jordi Girona 1-3, 08034 Barcelona, Spain

[4] Géoscience Montpellier, Université de Montpellier, CNRS, Montpellier, France

*Corresponding author:

Tybaud Goyetche

Institute of Environmental Assessment and Water Research (IDAEA), CSIC, Jordi Girona 18, 08034 Barcelona, Spain

e-mail: tgoyetche@gmail.com

Graphical abstract

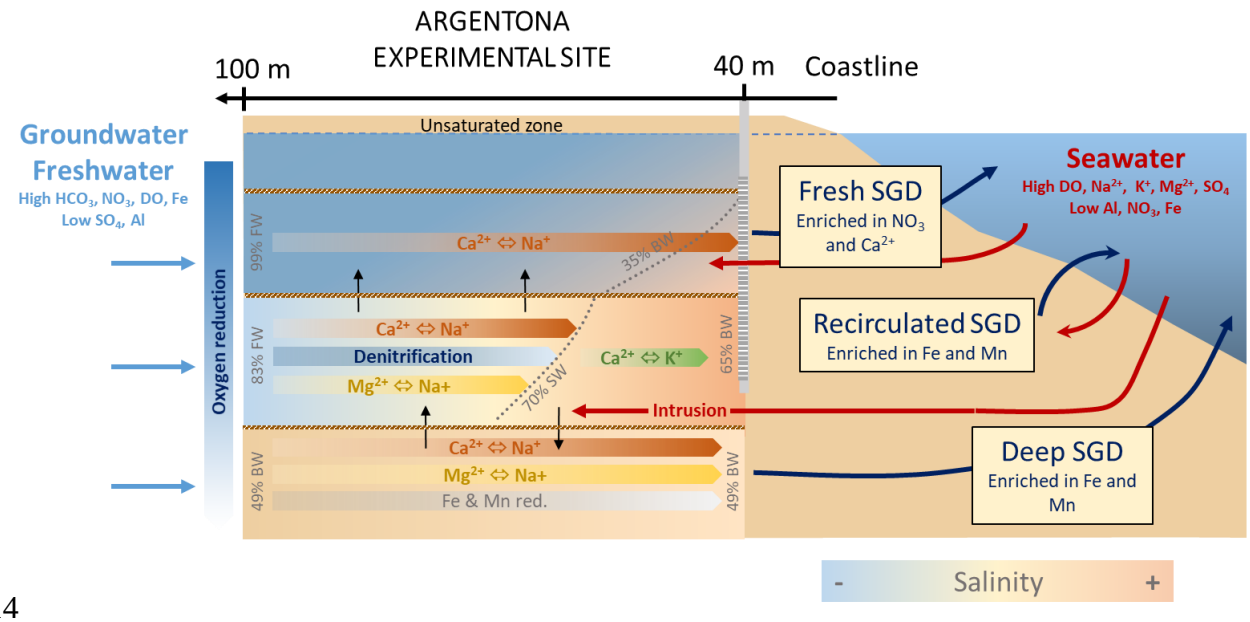

Highlights

- Coastal aquifers deliver large nutrient quantities to the sea through SGD.
- FW and SW mixing promotes numerous chemical reactions.
- Chemical reaction quantification is essential to assess GW quality SGD composition.
- Coastal aquifers play a significant role in contamination reduction.

Abstract

In coastal aquifers, two opposite but complementary processes occur: Seawater intrusion (SWI) and Submarine groundwater discharge (SGD). SWI may salinize freshwater in exploited aquifers while SGD transports essential chemical elements to the sea. Aquifers are expected to be chemically reactive, both because they provide abundant surfaces to catalyze reactions and because mixing the very different Fresh Water (FW) and SW should promote numerous reactions. Characterizing and quantifying these reactions are essential to assess the composition of both aquifer water quality and submarine groundwater discharge. Indeed, sampling SGD is difficult, so that its composition is usually uncertain. We propose a reactive mixing methodology based on principal component analysis to (i) identify the sources of water and possible reactions occurring in the aquifer, and (ii) quantify mixing ratios and the extent of chemical reactions. We applied this methodology to the Argentona coastal aquifer located North of Barcelona. The aquifer contains fluvial sediments of granitic origin and overlies weathered granite. Identification of end members (FW and SW) and the spatial distribution of their mixing ratios illustrate the application procedure. The extent of reactions and their spatial distribution allow us to distinguish reactions that occur as a result of SWI. This is relevant for recirculated saltwater SGD. The most important reaction is cation exchange, especially between Ca and Na, which promotes other

reactions such as gypsum and fluorite precipitation. Iron and Manganese are mobilized in the SW portion but oxidized and precipitated in the mixing zone, so that Fe (up to 15 μEq/L) and Mn (up to 10 μEq/L) discharge is restricted to SW SGD. Nitrate is reduced in the mixing zone. The actual reaction amounts are site specific, but the processes are not, which leads us to conjecture the importance of these reactions to understand the SGD discharge elsewhere.

Keywords

Grounwater; Coastal aquifer; Submarine Groundwater Discharge; Mixing model; EMMA Analysis; Chemical reactions.

1. Introduction

Population density in coastal areas is almost three times higher than the global average (Small & Nicholls, 2003). The impact of high population on freshwater (FW) demand is very strong. One of its consequences is the intensification of seawater (SW) intrusion (SWI) (Alfarrah & Walraevens, 2018). SWI is a natural coastal process that is intensified where there is a significant extraction of freshwater. At the same time, coastal aquifers discharge continental FW, largely mixed with SW in the aquifer, but also recirculated SW (Burnett et al., 2003) towards the sea through Submarine Groundwater Discharge (SGD). Some authors argue that the quantified volumes of SGD resulting from either recirculated SW (i.e. SW exchange resulting from sea level fluctuations), mixed FW and SW, or FW, are many times greater than the river discharge (Taniguchi et al., 2019). SGD carries high solute and nutrients concentrations into the sea (Slomp & Van Cappellen, 2004). Those elements may be important to submarine ecosystems (Luijendijk et al., 2020), which lends an added relevance to the hydrochemistry of coastal aquifers.

The hydrochemistry of coastal aquifers depends not only on the nature of the types of groundwater (end-members) that mix in these areas but also on their ensuing interactions and reactions with the solid phases (Moore, 1999). Numerous studies indicate the occurrence of chemical reactions in coastal aquifers including ion exchange, redox reactions related to organic matter biodegradation, and mineral dissolution and precipitation. Wigley and Plummer (1976) and Hanshaw and Back (1980) observed that the mixing between freshwater (FW) and seawater (SW), both in equilibrium with calcite, may tend to dissolve calcite, thus favoring coastal karst formation (Back et al., 1986; Fratesi, 2013). The fact that calcite dissolution has been reported with only 2% of SW (Magaritz et al., 1980), together with the fact that transport dynamics favor dissolution on the freshwater side of the mixing zone (Rezaei et al., 2005), not only explain karst development features, but also highlight the high reactivity that results from mixing so different waters.

Cation exchange, driven by the invasion of SW, is frequently reported as a leading geochemical process. A significant deviation of cations from conservative mixing (increases in calcium and decreases in sodium, magnesium, and potassium) is usually observed (Appelo & Willemsen, 1987; Giménez-Forcada, 2010; Gomis-Yagües et al., 2000; Martínez & Bocanegra, 2002; Pulido-Leboeuf, 2004). Russak et al. (2016) used field data and column experiments to study the effect of salinization and freshening cycles on other minor cations Li^{+}, B^{-}, Mn^{2+} and Ba^{2+}. Cation exchange, together with the dissolution of some minerals, can promote the precipitation of others. This is the case for dolomite and, especially, gypsum. In fact, a depletion in sulphate concentrations is observed in a majority of works (Andersen et al., 2005; A. P. Barker et al., 1998; Custodio, 1992; Gomis-Yagües et al., 2000). Sulphate reduction, which has also been proposed, requires anoxic conditions and significant amounts of electron donors, which

may be caused by naturally ocurring organic matter at the seabed or from polluted FW. In fact, iron and manganese reduction has been described in the mixing zone where microbial iron reduction has been proposed to account for most of the anaerobic degradation of natural organic matter (Snyder et al., 2004).

These biogeochemical reactions explain that the composition of submarine groundwater discharge differs from the one predicted by simple mixing of FW and SW (Moore, 2010). They also explain that saline water returning to the sea due to sea-aquifer exchange may be quite different from sea-water, which may help understanding sea chemical balances and SGD. For instance, the global calcium balance in the ocean has traditionally missed a significant input (Milliman, 1993; Wilkinson & Algeo, 1989), estimated between 40 and 120% of the fluvial inflow (Sawyer et al., 2016). Most research on SGD chemistry focuses on nutrients, which control primary production (Grzelak et al., 2018; Liu et al., 2021; Valiela et al., 1990). It has been found that commercial fish, aquaculture and lobster yields are positively correlated with terrestrial nutrients discharged into coastal waters (Peng et al., 2021; Sutcliffe Jr, 1972). Nutrients, which are essential elements for photosynthetic organisms and the ensuing trophic chains, may become harmful for submarine ecosystems and lead to algal blooms when in excess (Anderson et al., 2002; Chen et al., 2020; Luo & Jiao, 2016). Major ions cycles (Cl^-, SO_4^{2-}, Na^+, K^+, Mg^{2+}, Ca^{2+}, and HCO_3^-) attract relatively less attention because they are not limiting. Yet, they can exert a significant control on the chemical forcing in coastal areas and stimulate primary production (Kłostowska et al., 2020; Liu et al., 2017; Santos et al., 2008).

The large number and interdepence of chemical reactions in coastal aquifers makes their hydrochemistry difficult to explain. Hydro-chemical studies in coastal

aquifers are usually qualitative: describing groundwater composition and conjecturing the reactions that may lead to measured concentrations. We suggest that quantifying such potential reactions is useful to confirm or discard conceptual models, strengthen the analysis, and help to build numerical models. The quantification is traditionally achieved through models, which also help to assess the response of the system to changing conditions. But reactive transport models are conceptually difficult, because of difficulties of transport and density dependent flow, and practically complex, because they require a large amount of data and long observation time-series. To simplify the numerical model implementation, it is mandatory to identify the most important reactions.

A preliminary approximation to the concentrations of chemical species can be achieved using mixing models. These are based on writing the concentration of any species i in a sample j (C_{ij}) as (Christophersen et al., 1990; Hassen et al., 2018; Jurado et al., 2015) :

$$C_{ij} = \sum_{e} \lambda_{ej} C_{ei} \quad (1)$$

where C_{ei} is the concentration of species i in the end-member e and λ_{ej} is the proportion of end-member e in the sample j. λ_{ej} must satisfy the following constraints:

$$0 \leq \lambda_{ej} \leq 1 \quad (2)$$

$$\sum_{e} \lambda_{ej} = 1 \quad (3)$$

Mixing ratios can be obtained from the samples and end-members concentrations using these equations. The solution is trivial in the frequent cases where only two end-members (FW and SW) are present. In these cases, the fraction of seawater in sample j (λ_{SWj}) is classically calculated from Cl^- concentration (Appelo & Postma, 2005):

$$\lambda_{SWj} = \frac{C_{Cl,j} - C_{Cl,FW}}{C_{Cl,SW} - C_{Cl,FW}} \quad (4)$$

The large difference between Cl^- concentrations or similar salinity indicators, such as electrical conductivity, in FW and SW makes Eq. 4 quite robust and, thus, widely used. Still, attention must be paid to measurement errors, which can be identified if other species are used for the calculation of mixing ratios. For example, Shin et al. (2020) reported some underestimations using Br ions compared with Cl ions. Therefore, the chemical element chosen to calculate λ_{SWj} may be important. Conservative chemical elements such as stable isotopes, or metals are used as SWI and/or SGD tracers (Long & Valder, 2011; Nakaya et al., 2007). Other tracers (i.e. Sr and Ra isotopes) may help in computing mixing ratios but require specific sampling protocols and additional costs to regular monitoring campaigns. Moreover, the use of these tools can be hindered when the mixing between end-members is not clear, end-members composition vary with time or when they are not identified (Kendall & Caldwell, 1998, Cerdà-Domènech et al., 2017).

Identification of end-members is a conceptual problem. Often, they result from a good hydrogeological characterization of the system. Nevertheless, identification can be non-trivial in complex sites with multiple candidates for end-members. Identification is greatly aided by End Member Mixing Analysis (EMMA, Christophersen et al. (1990); Hooper (2003); Hooper et al. (1990); Vázquez-Suñé et al. (2010)). EMMA is a powerful statistical method based on principal component analysis (PCA) that aims at explaining the variability of a data set by reducing the dimensions of the problem by grouping correlated variables. To do so, eigenvalues are calculated and then projected into a low-dimensional space (2 or 3) by selecting the eigenvectors explaining most of the variability. End-members should encircle all the other projected observation points, which together with conceptual understanding helps in their identification. Once the end-

members have been identified, their mixing ratios in each sample can be evaluated. EMMA is an adequate technique, but cannot be directly applied to species that undergo some reaction. Therefore, a fairly widespread EMMA rule is to keep only the conservative species in the analysis (Li et al., 2016; Tubau et al., 2014), which is a limiting factor when many reactions occur and affect most species. This is particularly the case FW and SW mix, even if both are in equilibrium with the host sediments such as in coastal aquifers.

Including reactions in mixing calculations has been addressed by several researchers. Tubau et al. (2014) and Jurado et al. (2015) considered reactions as end-members by adding, for every reaction, an artificial end-member with the species participating in the reaction. Unfortunately, this approach does not properly represent mixing in the aquifer since the calculated mixing ratios do not add up to one (Eq. 3) and the identification of actual reactions remains unclear. Pelizardi et al. (2017) present a methodology to formalize mixing ratio calculations, which can be rewritten as:

$$C_{ij} = \sum_{e} \lambda_{ej} C_{ei} + \sum_{e} S_{ir}^{t} R_{rj} \qquad (5)$$

where S_{ir} is the stoichiometric coefficient of species i in reaction r and R_{rj} is the reaction extent of reaction r in sample j. That is, R_{rj} should be understood as the amount (expressed in moles or equivalents per liter) of reaction r reactants that have gone products in sample j. The method consists of several steps: (i) use the EMMA to identify the species participating in reactions and determine the associated reactions, (ii) define conservative components u associated with the reactions identified in the previous step (De Simoni et al., 2005), (iii) repeat the EMMA process with the conservative components for the identification of end-members and (iv) calculate the mixing ratios in each sample. The method is appealing because it formalizes the gist of hydrology (e.g., Davis and DeWiest (1966); Hurrell et al. (2013)): understanding water exchanges among

compartments (first term in Eq, 5) and the processes it undergoes (second term). Still, the method does not specify how to quantify the reactions (R_{rj}), and the methodology needs refinements on how to identify the reactions to be applied to real data (Pelizardi et al. (2017) examples are synthetic).

The objective of this work is double. First, we want to refine the reactive EMMA methodology and apply it to a complex real case influenced by SWI (the Argentona site, Martínez-Pérez et al. (2022)). Second, we want to identify and quantify hydrochemical processes at this coastal site to understand the chemistry of SGD.

2. Materials and methods

2.1.Study site, sampling, and analytical techniques

We use chemical data from the well-instrumented Argentona Experimental Site (Folch et al. 2020) located 30 km north of Barcelona (Spain), at the mouth of the Argentona ephemeral stream (Figure 1). This site is characterized by a dynamic SWI and SGD, which leads to an active mixing zone (Martínez-Pérez et al., 2022). The site climate is Mediterranean, with dry summers and mild, wet winters. Rainfall (some 600 mm/year) concentrates mainly during autumn and spring. It controls the Argentona stream flow and the alluvial aquifer recharge.

The site aims at monitoring seawater intrusion dynamics at different depths thanks to 15 wells. 12 of them form 4 nests with 2 m screened intervals at 3 different depths (15, 20, and 25 m). They are labeled Nx-15, Nx-20, and Nx-25 where x is the nest number (1 to 4). 3 other solitary boreholes complete the experimental site: PS-25 with a 2 m screened zone at 25 m depth and 2 fully screened boreholes of respectively 15 and 20 m depth (PP-15 and PP-20). The site is 100 m long inland from the coastline and 30 m wide.

The aquifer system is formed by alluvial deposits with an alternation of gravel, sands, and silty layers over a weathered granitic substratum. Mineralogy composition was measured through XRD at different depths and indicates a majority of silicates as Quartz (13–37%, SiO_2), Microcline (10–34%, $KAlSi_3O_8$), Albite (21–46%, $NaAl\ Si_3O_8$) and Fe rich Mg-hornblende (3–7%). Some clay minerals, such as Illite, are also observed with a fairly wide range depending on the depth (3–38%) (see details in Martínez-Pérez et al. (2022)). The anthropogenic impact in the watershed is quite significant with urban, agricultural, and industrial areas that can have an impact on groundwater quality (Rufí-Salís et al., 2019). Both the geological background and human activities in the watershed may foster reactions associated with the above minerals such as silicate alterations, cation exchange, and some organic matter degradation.

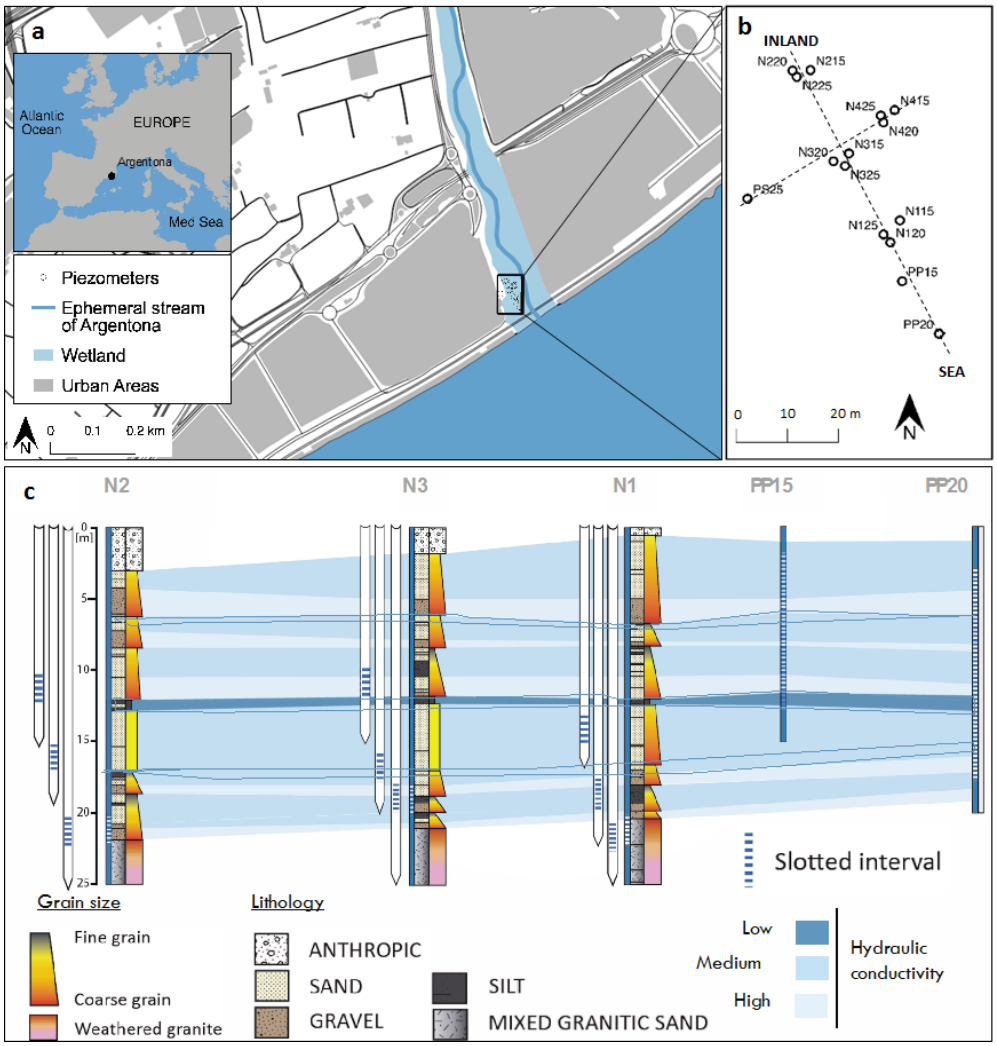

Figure 1: Experimental site of Argentona: (a) location, (b) borehole distribution, and (c) aquifer system (Modified from Martínez-Pérez et al. (2022))

Groundwater is sampled using submersible pumps (Gigant Submersible Pumps, Van Walt). A purging step is first applied by pumping at least three times the volume of the piezometer. Groundwater samples are then collected following a strict protocol and stored in pre-sanitized bottles. Sampling bottles had been previously washed with diluted nitric acid and rinsed with distilled water in the laboratory. Then in the field, each bottle is rinsed three times with groundwater before sampling and every other precaution is taken (use of gloves, handling one sample at a time, cleaning of utensils between taking each sample…) to avoid contamination. Electrical conductivity (EC), pH, temperature, Eh, and dissolved oxygen are measured on-site with a YSI multiparameter probe,

previously calibrated with standard solutions. These measurements are made through a flow cell to directly pass groundwater across sensors to avoid contact with ambient air and prevent degasification or mineral precipitation. Alkalinity (as HCO_3^-) is analyzed manually by tritration evaluation with sulfuric acid, accounting for the pH of the sample.

Table 1 summarizes the species analyzed for this study and the analytical method and laboratory. The water samples used for this study were collected during the field campaign of winter 2016 (presented in Martínez-Pérez et al. (2022)). As rains mainly occurs in autumn, we expect high FW content in groundwater samples. See supplementary materials for the full chemical dataset.

As the selected site is a coastal aquifer affected by SWI and SGD, the expected end-members for the mixing zone are, at least, one freshwater end-member representing the global aquifer water and seawater end-member (for the SWI part). As a representation of such end-members, we considered a well located on the Argentona watershed upper part for the freshwater (F1) and seawater (SW) from the nearby coast. To constrain all the possible water inflows in the Argentona site and to be sure to not exclude any potential end-members, we also sampled the ephemeral stream during a rainfall event (STREAM) and the wastewater treatment plant effluent (SEWAGE) that discharges in the sea near the experimental site.

Table 1 : Chemical species considered, analysis method, and laboratories of analysis.

Chemical species	Symbol	Analysis Method	Laboratory
Chloride	Cl^-	Ion Chromatography (IC)	Catalan Institute for Water Research (ICRA)
Sulphate	SO_4^{2-}		
Nitrate	NO_3^-		
Calcium (Ca)	Ca^{2+}	Inductively Coupled Plasma – Mass Spectrometry (ICP-MS)	Institute of Environmental Assessment and Water Studies (IDAEA)
Sodium (Na)	Na^+		
Magnesium (Mg)	Mg^{2+}		
Potassium (K)	K^+		
Manganese (Mn)	Mn^{2+}		
Iron (Fe)	Fe^{2+}		
Fluorine (F)	F^-		
Silicon (Si)	Si^{4+}		
Barium (Ba)	Ba^{2+}		
Bromine (Br)	Br^-		
Aluminium (Al)	Al^{3+}		
Lithium (Li)	Li^+		
$\delta^{18}O$ and δD	$\delta^{18}O$ and δD		University of Barcelona (UB).
Alkalinity (as HCO_3^-)	HCO_3^-	Titration-based	Field measurement
Electrical conductivity	EC	YSI multiparameter meter	Field measurement
Dissolved Oxygen	O_2	YSI multiparameter meter	Field measurement

2.2.Identification and quantification of chemical reactions

We propose a three step procedure for the identification and quantification of chemical reactions using reactive mixing calculations:

(1) Reactive EMMA for identification of reactions and end-members

(2) Mixing calculations

(3) Quantification of chemical reactions

These steps are detailed below.

2.2.1. Step 1: Reactive EMMA for identification of reactions and end-members

Interpretation and representation of hydrogeochemical data may be complex because of the large number of compounds and their time evolution. To simplify the analysis, the whole chemical data set is presented as a concentration matrix (X) ($n_s \times n$, where n_s is the number of chemical species and n is the number of samples). We used the application of EMMA-MIX (Carrera et al., 2004) to select end-members, evaluate the mixing ratios between different end-members and quantify the reactions occurring in the coastal aquifer of Argentona.

The identification of chemical reactions and end-members follows an iterative process, summarized in Figure 2:

Preliminary analysis: EMMA (Carrera et al., 2004) is applied to the original matrix X resulting from raw concentration data.

Step a: Propose candidate reactions: this is done by (1) conceptual analysis (some reactions, e.g., cation exchange may be expected to occur), (2) identification of species possibly participating in reactions by checking differences from expected conservative mixing behaviour. For example, the eigenvector associated to FW-SW mixing typically display contributions of around $1/\sqrt{n_s}$ for conservative species but not for those affected by chemical reactions, which tend to display a reduced contribution. Another typical example is the case of eigenvectors without clear end-members, but involving few species, which might come from a reaction (e.g., an eigenvector with large contributions to Ca^{2+} and SO_4^{2-} can indicate gypsum dissolution-precipitation).

Step b: **Build the stoichiometric matrix of the proposed reactions**. This matrix ($n_r \times n_s$, where n_r is the number of proposed reactions) includes the stoichiometric coefficient associated to species participating in the reactions.

Step c: Derive components (i.e., combinations of species that remain unchanged by the proposed reactions). This involves (1) computing the components matrix U ($n_s - n_r \times n_s$) from the stoichiometric matrix (see details in Pelizardi et al. (2017) and Molins et al. (2004)), and (2) multiplying the vector of concentrations of all species in each sample by the components matrix. This leads to a new data matrix, $X_u = U \cdot X$. In practice, this reduced data matrix results from eliminating the species involved in the reactions and replacing them with the corresponding components u, while keeping the species that do not participate in any reaction.

Step d: Conservative EMMA analysis: EMMA is repeated using X_u. In case new reactions are identified, the procedure is repeated until a significant percentage of the variance (say, more than 90%) can be explained by a few eigenvectors and the data projections are encircled by conceptually reasonable end-members.

In our analysis, described in detail in section 3.1, we identified 12 potential reactions in agreement with the geological context and human activities around the experimental site affecting our system:

$Ca^{2+} + SO_4^{2-} + 2H_2O \Leftrightarrow CaSO_4.2H_2O(s)$	Gypsum precipitation	(R_1)
$Na^+ + 0.5X_2Ca \Leftrightarrow 0.5Ca^{2+} + XNa$	Na – Ca Cation exchange	(R_2)
$K^+ + 0.5X_2Ca \Leftrightarrow 0.5Ca^{2+} + XK$	K – Ca Cation exchange	(R_3)
$Mg^{2+} + X_2Ca \Leftrightarrow Mg^{2+} + X_2Mg$	Mg – Ca Cation exchange	(R_4)
$CH_2O + O_2 \rightarrow HCO_3^- + H^+$	Aerobic respiration	(R_5)
$CH_2O + 0.8NO_3^- \rightarrow 0.4N_2 + HCO_3^- + 0.2H^+ + 0.4H_2O$	Denitrification	(R_6)
$2\,CH_2O + 4MnO_2 + 6H^+ \rightarrow 2HCO_3^- + 4Mn^{2+} + 4H_2O$	Manganese reduction	(R_7)
$CH_2O + 4FeO(OH) + 7H^+ \rightarrow HCO_3^- + 4Fe^{2+} + 6H_2O$	Iron reduction	(R_8)
$Ca^{2+} + 2F^- \Leftrightarrow CaF_2$	Fluorite precipitation.	(R_9)
$Ba^{2+} + SO_4^{2-} \Leftrightarrow BaSO_4$	Barite precipitation	(R_{10})

$KAlSi_3O_8 \rightarrow 3\,Si^{4+} + K^+ + Al^{3+}$ Feldspar weathering (R_{11})

$Al^{3+} + 3H_2O \Leftrightarrow Al(OH)_3 + 3H^+$ Gibbsite precipitation. (R_{12})

284 The 2 conservative components resulting from these reactions are:

$$u_1 = [Ca^{2+}] - [SO_4^{2-}] + 0.5[Na^+] + 0.5[K^+] + [Mg^{2+}] - 0.5[F^-] + [Ba^{2+}] + 1/6[Si^{4+}] \quad (6)$$

$$u_2 = [HCO_3^-] + [DO] + 1.25[NO_3^-] + 0.5[Mn^{2+}] + 0.25[Fe^{2+}] \quad (7)$$

285 where u_1 corresponds to the reactions associated to cation exchange and minerals
286 dissolution-precipitation affecting $[Ca^{2+}]$ while u_2 is associated to $[HCO_3^-]$ and redox
287 reactions. So, X_u is the matrix $(8 \times n)$ containing the two above components and the
288 remaining species not participating in reactions ($[\delta^{18}O]$, $[\delta D]$, $[EC]$, $[Br^-]$, $[Li^+]$ and
289 $[Cl^-]$).

290 **2.2.2. Step 2: Mixing calculations**

291 Once the end-members for each sample are identified using EMMA, mixing ratios
292 can be calculated using the MIX code (Carrera et al., 2004). A feature of this code is that
293 it acknowledges that the uncertainty of end-member compositions may be greater than
294 that of the actual samples. In essence, it is assumed that the measured concentrations,
295 C_{mij}, of species in sample j results from conservative mixing of n_e end-members (Eq. 1)
296 plus a measurement error and that the measured concentrations of end-members, C_{mei},
297 also contain errors. That is,

$$C_{mij} = \sum_{e=1}^{n_e} \lambda_{ej} C_{ei} + \varepsilon_{mij} \qquad i = 1, n_s; j = 1, n_m \quad (8a)$$

$$C_{mei} = C_{ei} + \varepsilon_{ei} \qquad i = 1, n_s; e = 1, n_m \quad (8b)$$

where ε_{mij} and ε_{ei} are the measurement errors of concentrations of mixtures (samples) and end-members, respectively. Mixing ratios, λ_{ej}, and end-member concentrations, C_{ei}, are obtained by minimizing the objective function:

$$F_{obj} = \sum_{i=1}^{n_s}\sum_{j=1}^{n_m}\left(\frac{\varepsilon_{mij}}{\sigma_{ij}}\right)^2 + \sum_{i=1}^{n_s}\sum_{e=1}^{n_e}\left(\frac{\varepsilon_{ei}}{\sigma_{ei}}\right)^2 \quad (9)$$

where σ_{ij} and σ_{ei} are the standard deviations of $\varepsilon_{mij}$and ε_{ei} respectively. These are the only data that needs to be specified, in addition to actual measurements, to run MIX. Here we have assigned by default a standard deviation of 0.1 times the measured concentration ($\sigma_{ij} = 0.1C_{ij}$), except for very small concentrations ($C_{mij} < 0.1\sigma_{si}$, where σ_{si} is the standard deviation of species i in all measurements), in which case σ_{ij} = $0.01\sigma_{si}$. The same criterion was initially applied to end-members. Variances can be adjusted to broaden or restrict the concentration calculations. To this end, it is convenient to verify the deviation of both end member and sample concentrations from the raw data to ensure that the projections of calculated end-members over the selected eigenvectors using EMMA (Figure 2e) encircle the samples. Otherwise, σ_{ei} can be adjusted so that the concentrations of the end-members do not deviate too much from conceptual expectations and the distribution is preserved.

In our case, we had to adjust σ_{ei} for the F1 sample for Cl^- and u_1. The initial values are respectively: 7.210 mmol/L ± 51.98 mmol/L and 1.881 mmol/L ± 528.59 mmol/L.

2.2.3. Step 3 : Quantification of chemical reactions

Once the e end-member proportions in sample j (λ_{ej}, Eq. 1) are calculated, we can quantify the extent of reaction R_{rj} in sample j (Step 3, Figure 2) from the

concentration of the secondary species associated to the reaction r (Eq. 4). We take advantage of the fact that we have built the stoichiometric matrices in such a way that a secondary species can only result from specific reaction. Therefore, the reaction extent R_{rj} of reaction r in sample j is equal to considering conservative mixing, the deviation from the measured concentration of species i ($C_{i_{Meas.}}$) from the conservative mixing concentrations (C_{rjm}) can be defined as (Eq. 5).

$$R_j = \left[C_{i_{Cons.}}\right] - [C_{i_{Meas.}}] \quad (0\text{-}10)$$

where $\left[C_{i_{Cons.}}\right]$ is calculated using λ_{ej} according to Eq. 1, as if there were no reactions (conservative mixing).

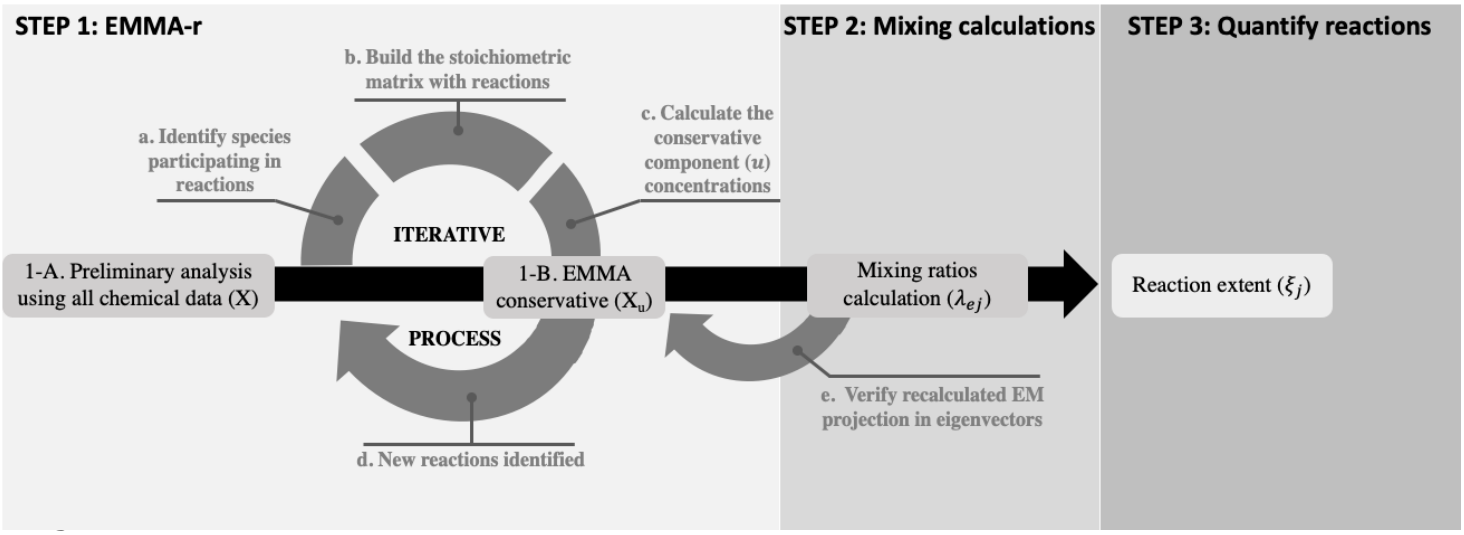

Figure 2: EMMA reactive flow chart for the end-member identification and chemical reactions quantification

3. Results and discussion

3.1.Step 1: Chemical reactions for end-member identification

In this section, we detail how we obtained the final chemical system applying the EMMA. We start (iteration 0) by consider all chemical species in Table 1The goal is to reduce the set of species and components through invoking reactions so as to explain.

Second, an iterative process begins until the variance by the least number of eigenvectors. Moreover, end-members must enclose the chemical composition of our system. Table 2 presents the parameters for each iteration and the results of the variance explained by EG1 and EG2.

Table 2 **:** Parameters varying in each iteration to identify chemical reactions using EMMA. Where n_r is the number of reactions considered, R_n the reaction identifier, n_s is the number of species considered, n_u is the number of conservative components, $W = \sqrt{1/(n_s + n_u)}$ is the theoretical contribution of each species, if all species and components were equally weighted, and n_e is the number of potential end-members identified.

Iteration number	0	1	2	3	4
$\boldsymbol{n_r}$	0	4	8	11	12
$\mathbf{R_n}$	-	R_1 to R_4	R_5 to R_8	R_9 to R_{11}	R_{12}
$\boldsymbol{n_s}$	20	15	10	6	6
$\boldsymbol{n_u}$	-	1	2	3	2
$\boldsymbol{W}$	0.22	0.25	0.29	0.33	0.35
$\boldsymbol{n_e}$	>4	4	4	3	2
EG1 contribution (%)	67.47	62.87	73.03	87.12	96.73
EG2 contribution (%)	11.53	13.96	11.50	10.43	2.10

Iteration 0 or preliminary analysis starts by applying the EMMA to the original chemical data without reactions (i.e., 20 x 18 matrix, both n_r and n_u are set to zero in Table 2). The two first eigenvectors explain 79% of the variance (Table 2). As shown in Figure 3a, EG1 represents the mixing between a freshwater end-member (FW) and the saline end-member (SW). However, we observe that many chemical species are affected by other processes than mixing. That is, their contribution is not equal to the theoretical contribution W of each species and components (with $W = \sqrt{1/(n_s + n_u)}$) if all were equally weighted (the values are shown in Table 2 and indicated in Figure 3, top row). Moreover, results show that more than two end-members are needed to explain a

significant portion of the data variability ($n_e > 4$, see Figure 3c). The results from this preliminary iteration (Iteration 0) imply that we must acknowledge chemical reactions to interpret groundwater hydrochemistry.

To acknowledge reactions, the first reactive EMMA (EMMA-reactive hereinafter) iteration (Iteration 1) includes cation exchange reactions (R2 to R4, Na^+, $K^+$and Mg^{2+} with Ca^{2+}) as they represent the main type of reaction occurring in non-karstic coastal aquifers (Russak & Sivan, 2010). We also included gypsum precipitation (R1) because it is frequently observed and because groundwater composition at the Argentona experimental site is depleted in SO_4^{2-} (Martínez-Pérez et al., 2022). Note, however, that results from the preliminary analysis (Iteration 0) did not suggest that the species participating in cation exchange or gypsum precipitation Na^+, K^+, Mg^{2+}, $SO_4^{2-}$and Ca^{2+},(indicated by a square in Figure 3a) are affected by any chemical reaction. Despite this, we have decided to include R1 to R4 in iteration 1 to highlight the importance of the conceptual model and the robustness of EMMA, allowing us to analyze and discuss the validity of chemical reactions.

Reacting species are eliminated from the data matrix X during EMMA-reactive iterations. Instead, conservative components (i.e. combinations of reactive species that remain unaffected by reactions) are added to X. In iteration 1, the conservative component resulting from cation exchange and gypsum precipitation is: $u_1 = Ca^{2+} - SO_4^{2-} + 0.5Na^+ + 0.5K^+ + Mg^{2+}$(see Supplementary Material). Results of iteration 1 demonstrate two things: (i) the variance explained by the first two eigenvectors is reduced to 77%, with a reduction of the EG1 relative contribution (see the difference with iteration 0 in Table 2); and (ii) we are still not able to identify end-members (Figure 3f). This lack of improvement reflects that we are not following the EMMA recommendations (i.e.

reduced contribution to the eigenvector representing mixing) when considering chemical reactions. In our case, EMMA suggests that we should consider other reactions first and possibly add R1 to R4 in a later iteration. Consequently, we added redox reactions affecting DO, NO_3^-, Mn^{2+}, and Fe^{2+} (indicated in Figure 3d) for iteration 2.

Adding redox reactions (R5 to R8) makes the chemical system more complex, with 8 chemical reactions ($n_r = 8$, Table 2) that lead to a second conservative component ($u_2 = HCO_3^- + DO + 1.25NO_3^- + 0.5Mn^{2+} + 0.25Fe^{2+}$) besides u_1, obtained from the previous iteration (see Supplementary Material). With two eigenvectors we are able to explain up to 85% of the variance (i.e., a of 6% gain over iteration 0). Nevertheless, it remains difficult to identify end-members (Figure 3i). New reactions are suggested by EG1, affecting Al^{3+}, F^-, Ba^{2+}, and Si^{4+}(see Figure 3g). These species and the mineral composition of the Argentona site, suggest adding fluorite, barite and feldspar mineral dissolution-precipitation reactions (R9 to R11). This leads to a third conservative component that $u_3 = Al^{3+} + 1/3\ Si^{4+}$(see Supplementary Material). u_3 represents the weathering of the granitic minerals present in the Argentona aquifer. Note that, since calcium and sulfate are already part of u_1, fluorite and calcite precipitation imply treating F^- and Ba^{2+} as secondary species and modifying u_1, which now reads : $u_1 = Ca^{2+} - SO_4^{2-} + 0.5Na^+ + 0.5K^+ + Mg^{2+} - 0.5F^- + Ba^{2+} + 1/6Si^{4+}$ and u_2 is unchanged.

The iterative process is repeated for a third time. According to this chemical system with 11 chemical reactions ($n_r = 11$), we explain 98% with 2 eigenvectors. This iteration gives better results than all the previous ones (+19% compared to iteration 0, Table 2). However, end-members identification remains unclear since it would be necessary to include 3 end-members to explain the data (F1, SW, and N1-25 as suggested in Figure 3l). The presence of 3 end-members in a case of seawater intrusion is not

400 unusual and has been described in several cases of study in the literature considering
401 different freshwater sources or some fossil seawater (Chatton et al., 2016; Eissa, 2018;
402 Kim et al., 2017; Sivan et al., 2005; Wicks & Herman, 1996). In our system, we see that
403 EG2 is mainly controlled by u_3 which corresponds to the granitic weathering. The fact is
404 that if R11, takes place, for each mole of weathered potassic feldspar, 3 moles of Si^{4+} and
405 1 mole of Al^{3+} should be added to the solution. But Al^{3+} is unstable in solution at pH >
406 5, which suggests that Aluminium should be precipitating. The questionable nature of the
407 third end-member and the excess of Al^{3+} prompted us to perform a 4th iteration by adding
408 Gibbsite (Aluminium hydroxide) precipitation (R12), (see Supplementary Material).

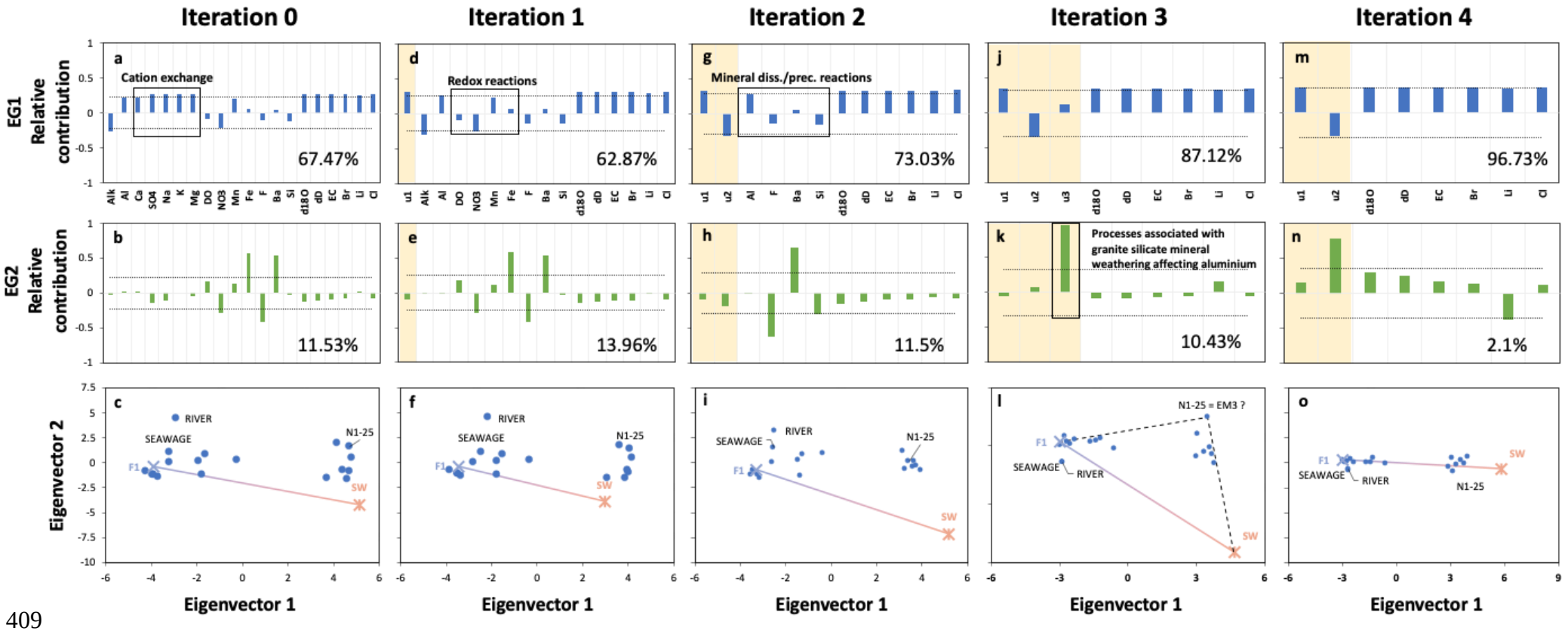

Figure 3 **:** Results of the EMMA iterative process for the identification of chemical reactions and end-members. Columns represent the iterations from left to right, going from 0 to 4, with the increasing number of reactions included in the chemical system. (1) species relative contribution to Eigenvector 1; (2) species relative contribution to Eigenvector 2 and (3) EMMA projection of concentration data defined by eigenvectors 1 and 2. Yellow vertical bands represent the number of conservative components involved in each iteration process.

This iteration proved to be the last one as it improved results, with 99% of the variance explained by the first 2 eigenvectors. But the greatest improvement is seen in Eigenvector 1 (EG1, Figure 3m), which explains almost 97%. Furthermore, we observe that almost all the species contribute equally with a relative weight of 0.35 ($\approx \sqrt{1/(n_s + n_u)}$), except u_2 which is anticorrelated (-0.35). As we indicated before, the EG1 direction is controlled by the mixing between freshwater and seawater. Accordingly, the u_2 anticorrelation with EG1 is quite consistent since the chemical species constituting u_2 (HCO_3^-, DO, NO_3^-, Mn^{2+}, Fe^{2+}, F^-) are representative of the freshwater with respect to other species. Moreover, in this last iteration, the relative contribution of Eigenvector 2 is reduced to 2% (see the reduction from iteration 0 to 4 in Table 2). EG2 is mainly characterized by the conservative component u_2 with a relative weight of 0.79. We consider the relative contribution of the remaining eigenvectors irrelevant since EG2 represents only 2% of the variance. From these results, the end-members are identifiable in the projection of sampling points using the first two eigenvectors. We observe an alignment of the points in the mixing line between F1 (freshwater end-member) and SW (Figure 3o).

3.2.Step 2: Mixing ratios and recalculated end members

Based on the iteration process, the model with 2 end-members (Iteration 4, Table 2) has been chosen for our data set. End-members exact composition of end-members is recalculated using the MIX code (Carrera et al., 2004) together with mixing ratios for each sample (Step 3, Figure 2). Table 3 presents the recalculated composition of end-members.

For $F1_r$, the code tends to reduce concentrations, more specifically for Li, Br, u_1, and EC. Changes are respectively: -100% (irrelevant concentration $1.44.10^{-6}$ mmol/L), -63%, -61%, -31%. This reduction suggests that the actual end-member might be closer to rainfall than any of our samples. In reality, MIX changes the concentrations to ensure that in this way, $F1_r$ and

439 SW_r encircle all the other samples in the projection of EG1 and EG2 (not presented here as it
440 overlays with the initial end-members). In the same way, to bring F1 closer to wells Nx-15 in
441 EG1 and EG2 projections, a slight increase in $\delta^{18}O$ and δD with respectively 3.6% and 2.4%.
442 While for SW_r, the most impacted concentrations are Li and u_2. The code tends to lower them
443 respectively by 58% and 48%. Furthermore, the EC rises from 53.00 mS/cm to 56.89 mS/cm.

444 The MIX code takes into account the variance indicated by the user to recalculate the
445 end-members. As mentioned before, as we were quite in agreement with the end-members
446 initial position, we had to reduce the degree of freedom for two species in F1: u_2 and Cl^-. So
447 that the code does not change too much the concentrations. In the case of totally unknown end-
448 members, this variance can be increased to assess the composition.

449 Table 3: Mix calculation chemical composition of the end-members. Units expressed in mmol/L for
450 chemical species and conservative components (u_1 and u_2) and mS/cm for EC.

	u_1	u_2	$\delta^{18}O$	δD	*EC*	*Br*	*Li*	*Cl*
Input end-members composition								
F1	6.972	7.210	-6.143	-37.527	0.980	0.011	0	1.881
SW	289.085	2.423	0.700	7.500	53.000	0.898	0.028	612.162
Output end-members composition								
$F1_r$	2.738	7.088	-5.92	-36.64	0.672	0.004	0	1.655
SW_r	287.983	1.262	0.684	6.627	56.894	0.883	0.012	552.43

451 The calculation also yields the proportion of each end-member in the observation wells
452 using (Table 4). Results are grouped by the proportion of FW. Group A (more than 90% FW)
453 includes all shallow piezometers, which is insistent with FW floating on top of SW. Group B
454 (between 70 and 90% FW) includes most intermediate depth wells. Finally, the remaining
455 samples are those of the deep and close to the shore piezometers. In summary, the observed
456 general trend is a decrease of the FW fraction with depth and from inland to the coast.

Table 4 : Calculated fraction of FW in Argentona experimental site from EC, Cl^- water molecule isotopes and mixing calculations indicates wells located on the transect parallel to the coastline, ** indicates fully screened wells.

		% $F1_r$ in samples			
Group	**Wells**	**EC**	**Cl**	**H_2O Isotopes**	**Mix code**
A	N2-15	99.7	99.9	98.6	99.7
	*N4-15	99.4	99.6	98.5	99.6
	N3-15	98.8	99.1	93.9	97.4
	N1-15	96.1	96.6	89.0	93.7
	**PP15	93.9	95.0	90.2	92.7
B	N2-20	80.6	83.4	84.4	88.2
	*N4-20	63.2	68.2	75.4	78.3
	N3-20	76.7	80.2	82.4	85.9
	**PP20-A	72.7	76.8	75.2	77.8
C	N2-25	26.5	30.0	34.1	33.3
	*PS-25	13.1	20.7	25.9	24.5
	*N4-25	11.0	18.1	19.8	18.3
	N3-25	12.1	19.5	19.8	18.4
	N1-25	25.2	30.3	34.3	34.9
	N1-20	4.2	14.2	9.2	8.7
	**PP20-B	15.4	23.9	23.7	22.7

The contribution to the objective function (F_{Ojb}) obtained by the MIX code after the mixing ratios end-members calculations are presented in Figure 4, classified by water sample (18), end-member (2), and chemical species (8). Note the largest contributions come from samples N1-15 (18%) and N3-15 (14%).

N1-15 is screened from 12.5 to 14.5 m, deeper than other boreholes belonging to the same group (Group A, Nx-15, from ~10 to 12 m). However, N1-15 is shallower than boreholes from Group B (Nx-20, from 15 to 17 m). Also, it is located just below a silt layer, identified at 12 m by Martínez-Pérez et al. (2022). Palacios et al. (2020) presents this silt layer as a hydraulic barrier affecting the mixing zone dynamics. Despite this, N1-15 presents 93.7% of $F1_r$ and a small SWr ratio that is reflecting a low penetration of the saltwater wedge at this sampling hydrologic condition.

MIX calculations for N3-15 pointed out a possible analytical error. $\delta^{18}O$ measured concentration is higher (-5.475 ‰) than the calculated concentration (-5.745 ‰). This calculated value is similar to another groundwater sampling campaign (-5.84 ‰), carried out one month later in the same well and with the same hydrological conditions. $\delta^{18}O$ is the chemical species with the highest contribution to the objective function and represents 35% of F_{Ojb} (Figure 4). The rest of the species have a low contribution to the objective function. The large contributions of stable isotopes to the objective function concentrate in the shallowest (freshest) samples, suggests that the high variability of stable isotopes in rainfall and exchange with surface water may not be well represented by a single freshwater end member.

		u1	u2	d18O	dD	EC	Br	Li	Cl	Total	Contribution to Fobj (%)
Normalized difference of end-members											
F1 vs F1r		-0.01	-0.08	-0.39	-0.14	-0.01	-0.02	-0.04	-0.01	-0.70	11.67
SW vs SWr		-0.12	0.00	0.00	-0.01	0.00	0.00	-0.16	-0.01	-0.29	4.87
Normalized difference of observation wells											
SEWAGE		0	0	0	0	0	0	0	0	0	0.00
RIVER		0	0	0	0	0	0	0	0	0	0.00
	N2-15	-0.001	-0.003	-0.001	-0.125	-0.01	-0.013	-0.011	0	-0.164	2.74
	*N4-15	0	-0.005	-0.013	-0.14	-0.016	-0.015	-0.073	0	-0.263	4.39
A	N3-15	0	-0.045	-0.575	-0.012	-0.039	-0.064	-0.008	-0.077	-0.82	13.69
	N1-15	-0.001	-0.097	-0.487	-0.149	-0.087	-0.076	-0.002	-0.187	-1.086	18.13
	**PP15	-0.001	-0.02	-0.125	0	-0.012	-0.007	-0.002	-0.042	-0.21	3.51
	N2-20	-0.006	-0.052	-0.195	-0.076	-0.058	-0.051	-0.009	-0.064	-0.511	8.53
B	*N4-20	-0.023	-0.056	-0.1	-0.037	-0.065	-0.053	-0.002	-0.073	-0.409	6.83
	N3-20	-0.01	-0.062	-0.1	-0.051	-0.059	-0.047	-0.055	-0.063	-0.446	7.44
	**PP20-A	-0.001	-0.004	-0.018	-0.019	-0.009	-0.003	-0.14	-0.009	-0.203	3.39
	N2-25	-0.033	-0.005	-0.002	-0.007	0	-0.002	-0.049	-0.01	-0.109	1.82
	*PS-25	-0.071	0	-0.009	-0.019	-0.002	-0.002	-0.001	-0.01	-0.114	1.90
	*N4-25	-0.001	0	-0.006	-0.007	0	0	-0.026	-0.005	-0.045	0.75
C	N3-25	-0.028	0	-0.006	-0.006	0	0	-0.019	-0.004	-0.063	1.05
	N1-25	-0.222	-0.005	-0.053	-0.023	-0.002	-0.003	-0.117	-0.012	-0.436	7.28
	N1-20	-0.064	0	0	-0.009	0	-0.001	-0.009	-0.001	-0.085	1.42
	**PP20-B	-0.028	0	-0.002	-0.002	0	0	0	-0.003	-0.036	0.60
Total		-0.619	-0.429	-2.081	-0.832	-0.373	-0.358	-0.726	-0.57	-5.991	
Contribution to Fobj (%)		10.33	7.16	34.74	13.89	6.23	5.98	12.12	9.51		

Figure 4**:** End-members and observation wells contribution to the objective function by species. Colored data bars are used to highlight the range of values, red colors to highlight observations maiximum by species and grey is used for totals). A longer bar represents a higher value.

485

3.3.Step 3: Quantification of chemical reactions

Mixing calculations have been performed using components that, according to our conceptual model, are conservative. We now use secondary species to calculate the extent of chemical reactions (R_{rj}, Eq. 5) as the deviation between the measured and calculated by simple mixing concentrations. The spatial distribution of R_{rj} expressed in mEq/L is presented in Figure 5 with positive (in red) and negative (in blue) values indicating the reaction direction, while wheat color represents weak or no reaction. As a reference, Figure 5 displays the measured electrical conductivity to identify the SWI distribution in the aquifer. Bear in mind that these reaction amounts do not reflect the local reaction rate but the integrated reactions that have occurred during GW transport since the end-member was sampled. As a result, one may conjecture that the extents computed for the most saline (nearly SW) samples reflect reactions that occurred shortly after sea water entered the aquifer.

Cation exchange reactions are the reactions with highest extent at the site. Specifically, R2 presents the highest extent of all reactions (up to 60 mEq/L). This implies that a lot of Ca^{2+} is desorbed to leave free sites for Na^{+}. This reaction is identified throughout the aquifer but probably occurs immediately after SW enters in contact with exchange sites. In fact, the extent of cation exchange (Na-Ca) is small in the inland and shallow part of the aquifer, where the fraction of SW is small. Note, however, that highest Na^{+}sorption does not occur at the most saline sample, but at the deepest part of the aquifer, in the seawater intrusion front, which we attribute to either kinetic control (the deepest samples are probably the oldest ones), to transport across weathered granite at the base of the aquifer, or to transient fluctuations of the SW front (see discussion for Magnessium below).

R3 displays lower extent values than R_2, and a maximum of 6 mEq/L of K^{+} is exchanged with Ca^{2+}. This reaction is also found mainly in the salty part of the aquifer (> 45

mS/cm). The last cation exchange reaction considered is Mg – Ca exchange (R4), which is found in the two directions, with some Mg^{2+}sorption ($R > 0$) up to 5.5 mEq/L and a strong desorption ($R < 0$) up to 30 mEq/L. Changes in magnesium concentration can only be attributed to sorption/desorption reactions as the Mg-rich minerals at the site, are a Mg-rich-hornblende and some biotite identified as trace and could not explain up to 30 mEq/L excess of Mg^{2+} by dissolution processes. Strong magnesium desorption is somewhat unexpected as $[Mg^{2+}]$ is already high in seawater. Mg^{2+}desorption occurs in the deep and middle aquifer portion in the inland part. At this same level, we observe the highest Na^{+}sorption values. Accordingly, we attribute the desorption of $Mg^{2+}$to transient exchange with Na^{+}. That is, Mg^{2+} that was sorbed in a previous freshening event may be desorbed when the SW front advances. In fact, salty samples often display more magnesium than would be expected from seawater (Kouzana et al., 2009; Mahlknecht et al., 2017; Shin et al., 2020). The release of chemical elements can be directly correlated with the ionic strength of the solution and the selectivity of a material for certain cations. Jiao and Post (2019) defined the selectivity sequence as $Na^{+} > K^{+} > Mg^{2+} > Ca^{2+}$, which coincides with the cation exchange sequence observed in Argentona. Na^{+} sorption in the front of the SWI, followed by the K^{+} in the salty part and the desorption of the Mg^{2+} a posteriori. Still, the most salient feature is the high sensitivity to salinity, which coupled to transient fluctuations explains anomalously high values of Mg^{2+} and Ca^{2+}.

R_1 displays positive values indicating that the release of calcium promotes the precipitation of gypsum. The large quantity of Ca^{2+} released during SW penetration, together with the high SO_4^{2-} in seawater (2907 mg/L) promotes the precipitation of gypsum. In this way, the area where gypsum will precipitate the most will be the area where Ca^{2+} is released, which explains why gypsum precipitation patterns are similar to Ca^{2+} desorption patterns. We observe that FW boreholes exhibit values close to 0 mEq/L of gypsum precipitation. This observation is in good agreement with Gomis-Yagües et al. (2000) that demonstrated the

535 possibility of gypsum precipitation at the salinity front during seawater intrusion. Note that
536 some sulfate concentration abatement could also be attributed to sulfate-reduction as mentioned
537 by Canfield (2001), a possibility we have not explored here.

538 For the discussion of redox reaction amounts, it is important to recall that Figure 5
539 should not be interpreted as a map of the place where reactions take place, but of the reaction
540 amounts required to explain the observed chemistry. Actual reactions may have occurred
541 anywhere along the way. The values associated to aerobic respiration reflect that we assume
542 SW to be initially fully oxygenated (~10 mg/l) as it is in equilibrium with the atmosphere while
543 freshwater dissolved oxygen is reduced due to aerobic reactions in the aquifer. We measured
544 low DO in deep boreholes (ranging from 0.1 to 1.5 mg/l) such as in PS25 and N4-25 which
545 imply that aerobic respiration (R5, Figure 5) has occurred. Nevertheless, we consider that this
546 reaction is probably not occurring in these boreholes but near the seafloor where organic matter
547 from dead marine biota is usually available.

548 Denitrification is also occurring as R6 > 0 (Figure 5). The reaction is mainly localized
549 in the middle and deep part of the aquifer section (Nx-20 and Nx-25 level). Unlike R5, where
550 oxygen comes from the sea, nitrate in R6 comes from FW, which explains why denitrification
551 is most apparent in the mixing zone. Mn reduction (R7) and Fe reduction (R8) display similar
552 patterns, with small reaction extents. Here, negative values indicate that Mn^{2+} and Fe^{2+} are
553 released to groundwater (probably reflecting reduction of ferric oxydes or dissolution of pyrite).
554 This occurs only in the deepest part of the aquifer, where O_2 is absent. Elsewhere, Mn and Fe
555 are oxidized. However, it appears that N3-25 stands out from other boreholes located at the
556 same depth. It forms a localized zone with reducing conditions, which has been observed by
557 various studies on other places (Brown et al., 1999; Chapelle & Lovley, 1992). For this well, a
558 higher proportion of clay was measured and a slower response to tidal fluctuations (Martínez-

559 Pérez et al., 2022). This may favor redox reactions due to lower groundwater circulation and/or
560 higher concentrations of iron oxides. In all, Mn^{2+} and Fe^{2+} appear to be mobilized during
561 intrusion but oxidized and precipitated in the mixing zone.

562 Finally, R9 to R10 are dissolution-precipitation processes or weathering of minerals.
563 Fluorite dissolution-precipitation is driven by the Calcium released by cation exchange.
564 Therefore, it is virtually absent in the FW portion and highest where calcium is highest. Both
565 R10 and R11, display negative values which indicate mineral dissolution. Barite dissolution
566 (R10) is very low (max 0.0046 mEq/L) and does not show a specific pattern. In the freshwater
567 part of the aquifer, *R* presents higher values (boreholes N2-15, N3-15, and N4-15). Feldspar
568 weathering (R11) is following the SWI shape with more alteration near the coast and increasing
569 with depth (up to 1 mEq/L). Note that the granite is less weathered at depth, and, thus, ready
570 for further alteration. As a consequence of feldspar alteration, Al tends to precipitate in the same
571 areas and in these pH conditions (pH>5, which destabilizes aluminum). We quantify Al
572 precipitation as gibbsite precipitation (R12) which is consistent with pH variability. Still, some
573 clay precipitation might also act as an Al sink.

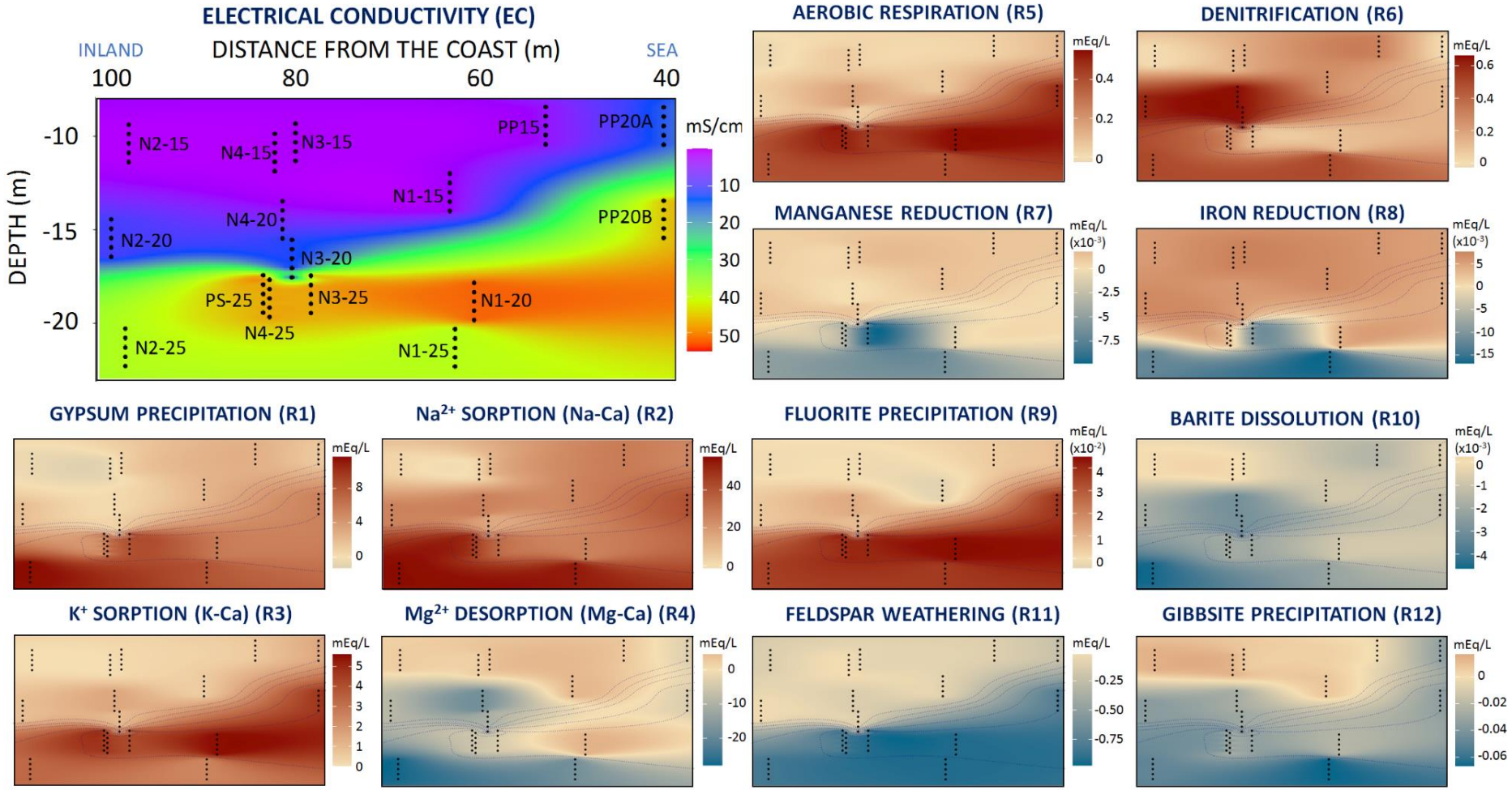

Figure 5**:** Chemical reaction amounts at the site samples. Note that the maps do not represent where the reactions take place, but the amount (mEq/L) needed to explain the observed concentrations. EC is displayed in the upper left as a SWI reference and dotted lines represent EC contours (15, 20, 25, 35, 45 mS/cm) in other subfigures.

3.4.Two end-members vs Three end-members accuracy

As presented in Section 3.1, the EMMA requires 3 end-members (Figure 3l) to explain 97.55% of the variance in iteration 3. Figure 6 presents a comparison between the reaction extent using 2 end-members (as presented in Figure 5) and 3 end-members (F1, SW, and N1-25, Figure 3l). We observe that, for most reactions, the reaction extent is reduced with respect to the case with 2 end-members. An average of 49% less gypsum (Figure 6a) and fluorite (Figure 6i) precipitate because calcium desorption (R2 to R4, Figure 6b, c, d) is reduced by an average of 31%. This is related to the 3rd end-member composition (recalculated based on N1-25 concentrations), which contributes with more Mg and less Na than seawater. Therefore, no competition between Na and Mg for exchange sites occurs, avoiding Mg desorption as it was occurring with 2 end-members (Figure 6d). The reductions of dissolved oxygen (Figure 6e) and denitrification (Figure 6f) are much lower (46% and 30% less) because they are already low in the 3rd end-member. So that the concentration reduction is caused by dilution instead redox reactions. We observe that using 3 end-members can lead to the opposite reaction as for R6 where negative R values are observed. With 2 end-members, Mn and Fe reduction (R7 and R8) were only affecting the deepest wells, and to a lesser extent Mn reduction was occurring at intermediate depths (Nx-20). However, if we consider three end-members, this manganese reduction is not observed and both Mn and Fe reduction are lower (40 and 50% less respectively). In the same way, considering a third end-member the barite dissolution and feldspar weathering are reduced by 37% and 57% respectively since the chemical compounds such as SO4, Ba, Si, and Al are modified by mixing processes. In conclusion, adding a third end-member minimizes the occurrence of chemical reactions.

These results illustrate the nature of our calculations. Computed reactions amounts reflect what is needed to explain derivations from mixing calculations. If an end-member has already suffered some reactions, the corresponding extents will implicitly accounted for by this

603 end member. In our case, both the 2 and 3 end-members models are valid representations of the
604 chemical system. But we prefer the 2 member calculation for parsimony, because it represents
605 two true end members (the third one is really a reacted mixture of the other two), and because
606 it represents better the actual reaction extents.

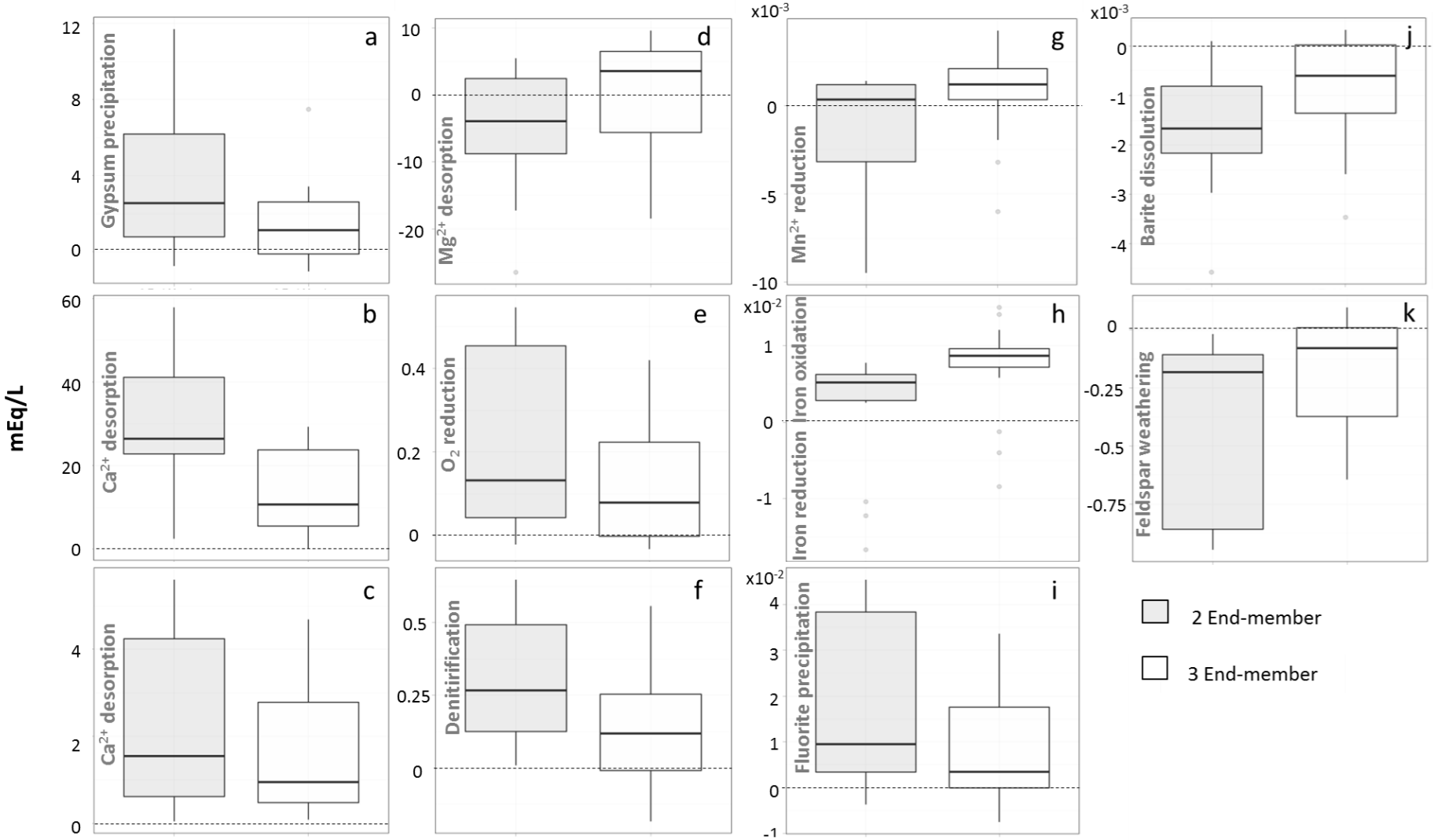

Figure 6**:** Comparison of reactions extent considering 2 end-members (gray) and 3 end-members (white)

3.5.Implications for SGD

It is well known that nutrients and pollutants are delivered into the coastal zone through SGD via submarine springs and seeps (B. Burnett, 1999; William C. Burnett, 1996; William C. Burnett et al., 2001; Monastersky, 1996). Yet, SGD contribution is often ignored for the assessment of biogeochemical cycles at the sea, mostly due to the lack of chemical data (Duque et al., 2020). Indeed, SGD samplings are difficult, except in karst environments, where the high flow rate of the submarine springs facilitate identification and sampling (Fleury et al., 2007). Elsewhere, SGD tend to be diffuse, which hinders sampling. This is especially true in alluvial aquifers and further complicated the spatio-temporal fluctuations of the discharge. Our method could address the limitations of direct sampling by determining how chemical reactions in the change the composition of SW and the easy to sample FW. The application to the Argentona site illustrates the high reactivity that can be found in coastal aquifers. It is worth stressing that we have identified reactions that occur to the three types of SGD: FW (Group A), mixed (Group B) and recirculated SW (Group C). FW is easy to characterixe by direct sampling. We were not surprised by the high reactivity of the mixing zone, which is expected to result from mixing two widely different waters (e.g., Wigley and Plummer, 1976; Rezaei et al., 2005). In hindsight, we should also have expected a high reactivity in the recirculated SW zone to result from SW-rock interactions.

For example, as mentioned previously, the simple mixing of end-members cannot explain the Ca^{2+} concentrations sampled in coastal aquifers since much more calcium is measured (Figure 7). At the Argentona experimental site, measured Ca^{2+} concentrations can reach 4 times the concentration measured in seawater. We attributed this concentration to desorption processes (i.e. cation exchange), attenuated by some gypsum and fluoride precipitation limiting Ca^{2+} concentration increase. We estimated that the

ratio of Ca^{2+} desorption-precipitation decreases from inland to the sea in groups B and C (Table 4.5), with an average of 8% ±4% and 19% ±8% respectively. This confirms that calcium will build up in SW immediately upon entrance in the aquifer. Ca^{2+} concentration in the sea is not very high (some 400 mg / L) and the oversaturation in calcite and other carbonate minerals means that the availability of Ca^{2+} is usually not a limiting element for the biological activity (Morse & Berner, 1995). Still, in laggons and/or closed areas, the calcium discharge can affect the carbonates balance. For example, Gattuso et al. (1998) demonstrated that coral calcification increases nearly 3-fold when aragonite saturation increases from 98% to 390%. Yet, the SW pH reduction associated to anthropogenic release of CO2 into the atmosphere is reducing carbonate concentration and the saturation states of biologically important calcium carbonate minerals (Barker & Ridgwell, 2012). Increased atmospheric CO2 is making Ca^{2+} inflows critical.

Nitrogen is a limiting element for photosynthetic organisms (plants or algae) in most oceans (~75%, Bristow et al., 2017). The N cycle has been dramatically altered by industrially fixed nitrogen by humans and wastewater discharge. We have seen that the aquifer plays an important role in the reduction of nitrates, through denitrification. Problems may appear when the nitrate rich FW discharges into the sea and denitrification is not sufficient to eliminate the nitrate overload, which may cause local eutrophication. No safe level of nitrate has been established for aquatic animals (Scott & Crunkilton, 2000; U. S. Environmental Protection Agency, 1986). The only existing limitation is for seawater culture with a maximum concentration of 20 mg NO3-N / l (Spotte (1979), indicated by a dotted line on Figure 7b). In the case of Argentona, if there were no reactions and nitrate concentration would be reduced by dilution only, this limit would be exceeded at all the shallow wells (N2-15, N3-15, and N4-15) where there is less than 5% SW, which may be cause eutrophication in closed lagoons (e.g., Velasco et al., 2006). But

denitrification reduces significantly nitrate concentrations (Figure 7), a limiting nutrient in oligotrophic seas. In either, denitrification is relevant.

Finally, seawater is characterized by low Fe (below 0.5 nM, Liu and Millero, 2002) because it tends to precipitate under aerobic conditions, so that river inflow is restricted to iron suspended particles. Yet, iron is an oligoelement that limits primary production in large portions of the ocean. For example, Fe loading from SGD has been shown to stimulate primary production in the South Atlantic Ocean (Windom et al., 2006). Fe requires reducing conditions to promote Fe mobility. The highest concentrations were measured in N1-25, N2-25 and N3-25 (0.61, 0.48 and 0.41 mg/L respectively), where we identified the highest iron reduction. Not surprisingly, these wells are deep and depleted in oxygen and nitrates, which has also been observed in Indonesia (Rusydi et al., 2021). In the rest of the wells, we observe that the concentrations are much lower than the conservative mixing line. Since our measurement of Fe in SW is anomalously high, we place little emphasis on Fe depletion in the saline portion. Instead, it is clear that some iron has been mobilized in the saline portion of the aquifer, and that this iron has been removed upon mixing with FW, which probably reflects oxidation and precipitation. A very similar comment can be made about Mn, which is “linked to nearly all other elemental cycles and intricately involved in the health, metabolism and function of the ocean's microbiome” (Hansel, 2017) and diplays very low concentrations in SW (less than 1 ppb, van Hulten et al.,2016). In short, both Fe and Mn may display significant concentrations in SW recirculated SGD, but probably not FW or mixed SGD. The fact that both elements are relatively abundant in the crust leads us to conjecture that SGD may be a significant source of Fe and Mn into the ocean.

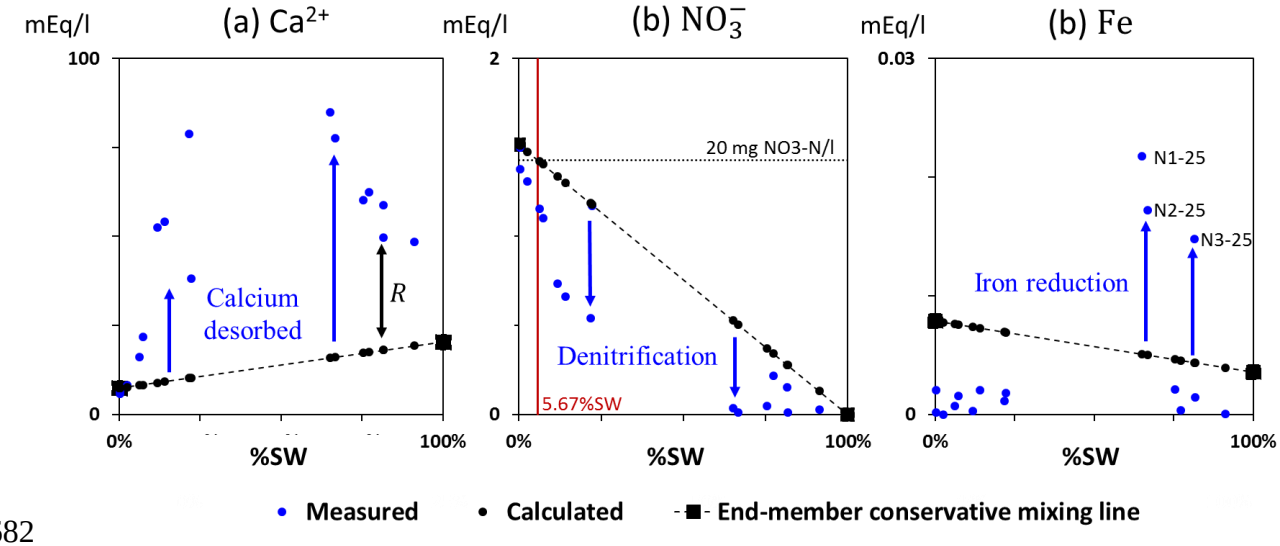

682

683 Figure 7: Production or loss of key elements (a: Ca^{2+}; b: NO_3; c: Fe) to SGD as a consequence of
684 geochemical reactions induced by mixing between FW and SW

4. Conclusion

685 End Member Mixing Analysis (EMMA), which has been traditionally associated
686 to the calculation of mixing ratios, is a promising tool to identify and quantify
687 hydrochemical processes occurring in both coastal and inland aquifers. In this work, we
688 described a detailed methodology to do so, and applied it to an alluvial coastal aquifer
689 (Argentona experimental site). We have deduced chemical reactions in the fresh, saline,
690 and mixing zone groundwater samples.

691 The complexity and high activity of coastal aquifers makes interpretation of
692 groundwater chemistry difficult. Application of the proposed reactive EMMA has
693 facilitated this task. Reactive EMMA reduces the dimension of the chemical system by
694 the use of conservative components instead of reactive chemical species, but removes the
695 dispersion caused by chemical reactions. At the Argentona site, this led to an increase of
696 the EMMA performance (reaching up to 97% of the variance explained by a single
697 eigenvalue, i.e., two end-members). This has facilitated computation of mixing ratios and
698 led to an overall robust performance. This easy methodology can be extended and

699 strongly recommended to other aquifers to understand processes taking place in each
700 geological/hydrogeological context (affecting compound released to the sea by SGD) and
701 also include it in temporal monitoring (i.e., progradation of carbonate dissolution in
702 karstic systems, trace contaminants discharge/retention and sources).

703 The EMMA has allowed us not only to obtain a consistent and simple
704 identification of end-members, but also to identify chemical reactions and to quantify
705 their extent. Chemical reaction identification and quantification for each sample
706 facilitates representing and understanding the spatial distribution of chemical processes
707 within the aquifer. Quantifying the reactions and where they occur allows not only to
708 know in which elements will SGD be enriched, but also to identify the composition of
709 each type of SGD (FW ouflow, SW recirculation, or mixed FW and SW).

710 We found that the highest reaction extent corresponds to cation exchange (up to
711 60 mEq of Ca^{2+} exchanged with Na^{+}). Calcium is a good example of the interdependence
712 of chemical reactions (involved directly or indirectly in 7 chemical reactions in our
713 system). This indicates that at least 8 species would have been removed from the chemical
714 system if we had adopted the traditional EMMA (only conservative species). On the other
715 extreme, we deduced other reactions, such as feldspar weathering or gibbsite
716 precipitation, which are probably more specific to our site but still relevant to understand
717 the origin of our samples and the processes undergone by GW.

718 While our quantitative results are site specific, we conjecture that many can be
719 expected elsewhere. Specifically, reducing conditions should be expected below the
720 seabed virtually everywhere due to dead biota. This will favor the mobilization of Fe and
721 Mn, which are important for ocean biochemical cycles. Cation exchange is ubiquitous
722 and should be expected in most places.

Supplementary materials

A. Hydrochemical data for EMMA analysis

n_s	1	2	3	4	5	6	7	8	9	10	11	12	13	14	15	16	17	18	19	20
Chemical species	**Alk**	**Al**	**Ca**	**SO4**	**Na**	**K**	**Mg**	**DO**	**NO3**	**Mn**	**Fe**	**F**	**Ba**	**Si**	**d18O**	**dD**	**EC**	**Br**	**Li**	**Cl**
Units	mmol/L	mmol/L	mmol/L	mmol/L	mmol/L	mmol/L	mmol/L	mmol/L	mmol/L	mmol/L	mmol/L	mmol/L	mmol/L	mmol/L	‰	‰	mS/cm	mmol/L	mmol/L	mmol/L
F1	5.279	0.005	3.668	1.072	4.703	0.064	1.943	0.035	1.516	0.001	0.004	0.010	0.000	0.329	-6.143	-37.527	0.980	0.011	0.000	1.881
SW	2.098	0.008	10.233	30.259	489.071	9.890	59.659	0.324	0.000	0.000	0.002	0.057	0.000	0.004	0.700	7.500	53.000	0.898	0.028	612.162
N1-25	1.901	0.030	42.429	16.037	265.893	3.916	48.146	0.025	0.037	0.004	0.011	0.004	0.001	0.354	-1.700	-8.100	39.900	0.621	0.016	427.055
SEWAGE	4.918	0.000	0.158	0.015	0.110	0.009	0.016	0.032	0.006	0.000	0.001	0.001	0.000	0.285	-6.185	-37.804	0.600	0.000	0.000	0.047
RIVER	4.918	0.000	0.818	0.068	0.482	0.345	0.582	0.032	0.105	0.000	0.018	0.004	0.003	0.285	-6.154	-37.599	0.880	0.000	0.000	0.241
PP15	4.902	0.006	10.882	1.837	11.733	0.146	4.616	0.036	1.102	0.000	0.001	0.009	0.001	0.336	-5.310	-33.522	4.140	0.061	0.001	32.558
PP20A	4.602	0.017	19.060	6.929	87.109	0.720	16.297	0.047	1.171	0.000	0.001	0.014	0.001	0.313	-4.500	-26.700	15.190	0.215	0.001	143.759
N1-15	5.502	0.003	8.067	1.714	9.757	0.134	3.120	0.022	1.154	0.000	0.000	0.017	0.001	0.330	-5.252	-32.992	2.990	0.043	0.001	22.537
N3-15	5.102	0.003	4.108	1.462	5.414	0.145	1.535	0.028	1.310	0.000	0.000	0.013	0.000	0.338	-5.475	-35.235	1.580	0.015	0.001	7.210
N4-15	5.502	0.001	3.317	1.561	4.125	0.049	1.121	0.007	1.379	0.000	0.000	0.010	0.000	0.332	-5.933	-37.330	1.290	0.013	0.001	4.042
N2-15	4.802	0.000	2.921	1.480	3.661	0.050	0.979	0.046	1.500	0.000	0.001	0.012	0.000	0.360	-5.890	-37.350	1.120	0.012	0.000	2.499
PP20B	3.101	0.019	31.176	20.956	338.865	2.950	48.337	0.016	0.219	0.000	0.000	0.009	0.001	0.272	-0.800	-3.300	45.000	0.680	0.009	466.107
N1-20	2.701	0.016	24.268	24.768	420.467	3.437	51.880	0.025	0.027	0.001	0.000	0.008	0.001	0.268	0.100	3.300	50.800	0.768	0.010	525.340
N3-20	4.602	0.016	27.094	4.783	57.205	0.431	15.226	0.053	0.663	0.000	0.001	0.009	0.002	0.311	-5.100	-30.000	13.090	0.184	0.001	122.992
N4-20	4.101	0.015	39.368	7.255	83.429	0.634	23.050	0.016	0.539	0.001	0.001	0.009	0.002	0.292	-4.600	-26.800	20.100	0.288	0.003	195.685
N2-20	4.802	0.018	26.207	3.607	35.699	0.336	12.883	0.053	0.734	0.000	0.000	0.011	0.001	0.299	-5.300	-30.900	11.080	0.158	0.001	103.385
N3-25	2.801	0.019	24.821	20.760	366.816	3.914	51.161	0.048	0.155	0.005	0.007	0.008	0.001	0.298	-0.500	-1.500	46.700	0.723	0.012	493.298
N4-25	2.401	0.016	29.363	21.385	356.742	3.636	52.437	0.014	0.010	0.002	0.001	0.007	0.001	0.287	-0.500	-1.500	47.300	0.734	0.013	502.001
N2-25	2.501	0.024	38.779	14.683	269.921	3.267	53.693	0.032	0.010	0.003	0.009	0.006	0.002	0.323	-1.500	-8.000	39.200	0.628	0.012	428.945
PS25	1.891	0.022	30.061	21.048	320.761	2.628	48.101	0.003	0.046	0.002	0.001	0.007	0.001	0.279	-0.900	-4.300	46.200	0.710	0.010	485.614

724

B. Iteration 1: Stoichiometric and component matrix for cation exchange and gypsum precipitation

We start from a chemical system governed by four chemical reactions (n_r = 4), with cation exchange (Na-Ca, K-Ca and Mg-Ca) and gypsum precipitation. We defined SO_4, Na, K and Mg as secondary species. Such that the stoichiometric matrix can be writen as: $S = (S_1|-I)$. The secondary species have to coincides with the opposite of the identity matrix, I. For this first chemical system the stoichiometric matrix is:|

	Stoichiometric matrix		1 Alk	2 Al	3 Ca	4 DO	5 NO3	6 Mn	7 Fe	8 F	9 Ba	10 Si	11 SO4	12 Na	13 K	14 Mg
R1	Ca - yeso = SO4	R1	0	0	-1	0	0	0	0	0	0	0	-1	0	0	0
R2	Na + 0.5X-Ca =X-Na + 0.5Ca	R2	0	0	0.5	0	0	0	0	0	0	0	0	-1	0	0
R3	K + 0.5X-Ca =X-K + 0.5Ca	R3	0	0	0.5	0	0	0	0	0	0	0	0	0	-1	0
R4	Mg + X-Ca = Ca - X-Mg	R4	0	0	1	0	0	0	0	0	0	0	0	0	0	-1
			Primary species										Secondary species			

The component matrix (U) is then obtained by transforming the stoichiometric matrix as follows $U = (I|S_u^t)$. The obtained component matrix for iteration 1 is:

	Components matrix		Alk	Al	Ca	DO	NO3	Mn	Fe	F	Ba	Si	SO4	Na	K	Mg
	Alk	1	1	0	0	0	0	0	0	0	0	0	0	0	0	0
	Al	2	0	1	0	0	0	0	0	0	0	0	0	0	0	0
u1	Ca-SO4+0.5Na+0.5K+Mg	3	0	0	1	0	0	0	0	0	0	0	-1	0.5	0.5	1
	DO	4	0	0	0	1	0	0	0	0	0	0	0	0	0	0
	NO3	5	0	0	0	0	1	0	0	0	0	0	0	0	0	0
	Mn	6	0	0	0	0	0	1	0	0	0	0	0	0	0	0
	Fe	7	0	0	0	0	0	0	1	0	0	0	0	0	0	0
	F	8	0	0	0	0	0	0	0	1	0	0	0	0	0	0
	Ba	9	0	0	0	0	0	0	0	0	1	0	0	0	0	0
	Si	10	0	0	0	0	0	0	0	0	0	1	0	0	0	0

In this first iteration, one conservative component is obtained such that: $u_1 = Ca^{2+} - SO_4^{2-} + 0.5Na^+ + 0.5K^+ + Mg^{2+}$. Then the same process is repeated for each chemical system, where new chemical reactions are included in the stoichiometric matrix.

C. Iteration 2: Stoichiometric and component matrix for redox reactions

The stoichiometric matrix is:

	Stoichiometric matrix		1 Alk	2 Al	3 Ca	4 F	5 Ba	6 Si	7 SO4	8 Na	9 K	10 Mg	11 DO	12 NO3	13 Mn	14 Fe
R1	Ca - yeso = SO4	R1	0	0	-1	0	0	0	-1	0	0	0	0	0	0	0
R2	Na + 0.5X-Ca =X-Na + 0.5Ca	R2	0	0	0.5	0	0	0	0	-1	0	0	0	0	0	0
R3	K + 0.5X-Ca =X-K + 0.5Ca	R3	0	0	0.5	0	0	0	0	0	-1	0	0	0	0	0
R4	Mg + X-Ca = Ca - X-Mg	R4	0	0	1	0	0	0	0	0	0	-1	0	0	0	0
R5	Redox O2	R5	1	0	0	0	0	0	0	0	0	0	-1	0	0	0
R6	Redox NO3	R6	1.25	0	0	0	0	0	0	0	0	0	0	-1	0	0
R7	Redox Mn	R7	0.5	0	0	0	0	0	0	0	0	0	0	0	-1	0
R8	Redox Fe	R8	0.25	0	0	0	0	0	0	0	0	0	0	0	0	-1

Primary species Secondary species

742

743 The component matrix is:

	Components matrix		Alk	Al	Ca	F	Ba	Si	SO4	Na	K	Mg	DO	NO3	Mn	Fe
u2	Alk + DO + 1.25NO3 + 0.5Mn + 0.25Fe	1	1	0	0	0	0	0	0	0	0	0	1	1.25	0.5	0.25
	Al	2	0	1	0	0	0	0	0	0	0	0	0	0	0	0
u1	Ca - SO4 + 0.5Na + 0.5K + Mg	3	0	0	1	0	0	0	-1	0.5	0.5	1	0	0	0	0
	F	4	0	0	0	1	0	0	0	0	0	0	0	0	0	0
	Ba	5	0	0	0	0	1	0	0	0	0	0	0	0	0	0
	Si	6	0	0	0	0	0	1	0	0	0	0	0	0	0	0

744

745 A new conservative component is obtained : $u_2 = HCO_3^- + DO + 1.25NO_3^- +$

746 $0.5Mn^{2+} + 0.25Fe^{2+}$.

747 **D. Iteration 3: Stoichiometric and component matrix for minerals dissolution-**

748 **precipitation reactions**

749 The stoichiometric matrix is:

	Stoichiometric matrix		1 Alk	2 Al	3 Ca	4 SO4	5 Na	6 K	7 Mg	8 DO	9 NO3	10 Mn	11 Fe	12 F	13 Ba	14 Si
R1	Ca - yeso = SO4	R1	0	0	-1	-1	0	0	0	0	0	0	0	0	0	0
R2	Na + 0.5X-Ca =X-Na + 0.5Ca	R2	0	0	0.5	0	-1	0	0	0	0	0	0	0	0	0
R3	K + 0.5X-Ca =X-K + 0.5Ca	R3	0	0	0.5	0	0	-1	0	0	0	0	0	0	0	0
R4	Mg + X-Ca = Ca - X-Mg	R4	0	0	1	0	0	0	-1	0	0	0	0	0	0	0
R5	Redox O2	R5	1	0	0	0	0	0	0	-1	0	0	0	0	0	0
R6	Redox NO3	R6	1.25	0	0	0	0	0	0	0	-1	0	0	0	0	0
R7	Redox Mn	R7	0.5	0	0	0	0	0	0	0	0	-1	0	0	0	0
R8	Redox Fe	R8	0.25	0	0	0	0	0	0	0	0	0	-1	0	0	0
R9	F + 1/2Ca = 1/2CaF3	R9	0	0	-0.5	0	0	0	0	0	0	0	0	-1	0	0
R10	Ba + SO4 = BaSO4	R10	0	0	1	0	0	0	0	0	0	0	0	0	-1	0
R11	Si = 1/3Feldspath Alteration - 1/3K - 1/3 Al	R11	0	0.33	0.17	0	0	0	0	0	0	0	0	0	0	-1

Primary species Secondary species

750

751 The component matrix is:

			Alk	Al	Ca	SO4	Na	K	Mg	DO	NO3	Mn	Fe	F	Ba	Si
u2	**Alk** + DO +1.25NO3 + 0.5Mn + 0.25Fe	1	1	0	0	0	0	0	0	1	1.25	0.5	0.25	0	0	0
u3	**Al** + 0.33 Si	2	0	1	0	0	0	0	0	0	0	0	0	0	0	0.33
u1	**Ca** - SO4 + 0.5Na + 0.5K + Mg -0.5F + Ba + 1/6Si	3	0	0	1	-1	0.5	0.5	1	0	0	0	0	-0.5	1	0.17

752

753 A new conservative component is obtained : $u_3 = Al^{3+} + 1/3Si^{4+}$ and the

754 conservatives components u_1 and u_2 now reads as follows: $u_1 = Ca^{2+} - SO_4^{2-} +$

755 $0.5Na^+ + 0.5K^+ + Mg^{2+} - 0.5F^- + Ba^{2+} + 1/6Si^{4+}$. u_2 is identical to the previous

756 iteration: $u_2 = HCO_3^- + DO + 1.25NO_3^- + 0.5Mn^{2+} + 0.25Fe^{2+}$.

E. Iteration 4: Stoichiometric and component matrix for gibbsite precipitation

The stoichiometric matrix is:

		1	2	3	4	5	6	7	8	9	10	11	12	13	14
Stoichiometric matrix		**Alk**	**Ca**	**SO4**	**Na**	**K**	**Mg**	**DO**	**NO3**	**Mn**	**Fe**	**F**	**Ba**	**Si**	**Al**
Ca - yeso = SO4	**R1**	0	-1	-1	0	0	0	0	0	0	0	0	0	0	0
Na + 0.5X-Ca =X-Na + 0.5Ca	**R2**	0	0.5	0	-1	0	0	0	0	0	0	0	0	0	0
K + 0.5X-Ca =X-K + 0.5Ca	**R3**	0	0.5	0	0	-1	0	0	0	0	0	0	0	0	0
Mg + X-Ca = Ca - X-Mg	**R4**	0	1	0	0	0	-1	0	0	0	0	0	0	0	0
Redox O2	**R5**	1	0	0	0	0	0	-1	0	0	0	0	0	0	0
Redox NO3	**R6**	1.25	0	0	0	0	0	0	-1	0	0	0	0	0	0
Redox Mn	**R7**	0.5	0	0	0	0	0	0	0	-1	0	0	0	0	0
Redox Fe	**R8**	0.25	0	0	0	0	0	0	0	0	-1	0	0	0	0
F + 1/2Ca = 1/2CaF3	**R9**	0	-0.5	0	0	0	0	0	0	0	0	-1	0	0	0
Ba + SO4 = BaSO4	**R10**	0	1	0	0	0	0	0	0	0	0	0	-1	0	0
Si = 1/3Feldspath Alteration - 1/3K - 1/3 Al	**R11**	0	0.17	0	0	0	0	0	0	0	0	0	0	-1	0
Al --> Gibbsite	**R12**	0	0	0	0	0	0	0	0	0	0	0	0	0	-1

Primary species Secondary species

The component matrix is:

			Alk	Ca	SO4	Na	K	Mg	DO	NO3	Mn	Fe	F	Ba	Si	Al
u2	**Alk** + DO +1.25NO3 + 0.5Mn + 0.25Fe	**1**	1	0	0	0	0	0	1	1.25	0.5	0.25	0	0	0	0
u1	**Ca** - SO4 + 0.5Na + 0.5K + Mg -0.5F + Ba + 1/6Si	**2**	0	1	-1	0.5	0.5	1	0	0	0	0	-0.5	1	0.17	0

During this iteration, u_3 is removed and only and the conservatives components u_1 and u_2 remain unchanged.

Acknowledgements:

This work has been funded by the Spanish Government through MEDISTRAES III projects (grant nos. PID2019-110212RB-C22 and PID2019-110311RB-C21), LOGIC project (grant no. RTC2019-007484-5) and IDAEA-CSIC Center of Excellence Severo Ochoa (Grant CEX2018-000794-S). This work is also part of the project TerraMar (grant no. ACA210/18/00007) of the Catalan Water Agency. We also acknowledge the Spanish Ministry of Economy, Industry and Competitiveness for the PhD fellowship (BES-2017-080028) from the FPI Program awarded to T. Goyetche. The author A. Folch is a Serra Húnter Fellow.

Bibliography

Alfarrah, N., & Walraevens, K. (2018). Groundwater overexploitation and seawater intrusion in coastal areas of arid and semi-arid regions. *Water, 10*(2), 143.

Andersen, M. S., Nyvang, V., Jakobsen, R., & Postma, D. (2005). Geochemical processes and solute transport at the seawater/freshwater interface of a sandy aquifer.

Geochimica et Cosmochimica Acta, 69(16), 3979-3994. doi:https://doi.org/10.1016/j.gca.2005.03.017

Anderson, D. M., Glibert, P. M., & Burkholder, J. M. (2002). Harmful algal blooms and eutrophication: nutrient sources, composition, and consequences. *Estuaries, 25*(4), 704-726.

Appelo, C. A. J., & Postma, D. (2005). Geochemistry. *Groundwater and pollution, 536*.

Appelo, C. A. J., & Willemsen, A. (1987). Geochemical calculations and observations on salt water intrusions, I. A combined geochemical/minxing cell model. *Journal of Hydrology*, *94*(3-4), 313-330.

Armstrong, F. A. J. (1957). The iron content of sea water. *Journal of the Marine Biological Association of the United Kingdom, 36*(3), 509-517.

Back, W., Hanshaw, B. B., Herman, J. S., & Van Driel, J. N. (1986). Differential dissolution of a Pleistocene reef in the ground-water mixing zone of coastal Yucatan, Mexico. *Geology*, *14*(2), 137-140.

Barker, A. P., Newton, R. J., Bottrell, S. H., & Tellam, J. H. (1998). Processes affecting groundwater chemistry in a zone of saline intrusion into an urban sandstone aquifer. *Applied Geochemistry, 13*(6), 735-749. doi:https://doi.org/10.1016/S0883-2927(98)00006-7

Barker, S., & Ridgwell, A. (2012). Ocean acidification. *Nature Education Knowledge, 3*(10), 21.

Bristow, L. A., Mohr, W., Ahmerkamp, S., & Kuypers, M. M. M. (2017). Nutrients that limit growth in the ocean. *Current Biology, 27*(11), R474-R478.

Brown, C. J., Coates, J. D., & Schoonen, M. A. A. (1999). Localized Sulfate-Reducing Zones in a Coastal Plain Aquifer. *Groundwater, 37*(4), 505-516.

Burnett, B. (1999). Offshore springs and seeps are focus of working group. *Eos, Transactions American Geophysical Union, 80*(2), 13-15.

Burnett, W. C. (1996). Tracing groundwater flow into surface waters using natural super (222) RN. *LOICZ Reports Studies*(8), 22-36.

Burnett, W. C., Bokuniewicz, H., Huettel, M., Moore, W. S., & Taniguchi, M. (2003). Groundwater and pore water inputs to the coastal zone. *Biogeochemistry, 66*(1), 3-33.

Burnett, W. C., Taniguchi, M., & Oberdorfer, J. (2001). Measurement and significance of the direct discharge of groundwater into the coastal zone. *Journal of Sea Research, 46*(2), 109-116.

Canfield, D. (2001). Biogeochemistry of sulfur isotopes. *Reviews in mineralogy and geochemistry, 43*(1), 607-636.

Carrera, J., Vázquez-Suñé, E., Castillo, O., & Sánchez-Vila, X. (2004). A methodology to compute mixing ratios with uncertain end-members. *Water Resources Research, 40*(12).

Cerdà-Domènech, M., Rodellas, V., Folch, A., & Garcia-Orellana, J. (2017). Constraining the temporal variations of Ra isotopes and Rn in the groundwater end-member: Implications for derived SGD estimates. Science of the total environment, 595, 849-857.

Custodio, E. (1992). Coastal aquifer salinization as a consequence of aridity: the case of Amurga phonolitic massif, Gran Canaria Island. *Study and Modelling of Salwater Intrusion, CIMNE-UPC, Barcelona*, 81-98.

Chapelle, F. H., & Lovley, D. R. (1992). Competitive exclusion of sulfate reduction by Fe (lll)-reducing bacteria: a mechanism for producing discrete zones of high-iron ground water. *Groundwater, 30*(1), 29-36.

826 Chatton, E., Aquilina, L., Pételet-Giraud, E., Cary, L., Bertrand, G., Labasque, T., . . .
827 Pauwels. (2016). Glacial recharge, salinisation and anthropogenic contamination
828 in the coastal aquifers of Recife (Brazil). *Science of The Total Environment, 569-*
829 *570*, 1114-1125. doi:https://doi.org/10.1016/j.scitotenv.2016.06.180
830 Chen, X., Cukrov, N., Santos, I. R., Rodellas, V., Cukrov, N., & Du, J. (2020). Karstic
831 submarine groundwater discharge into the Mediterranean: Radon-based nutrient
832 fluxes in an anchialine cave and a basin-wide upscaling. *Geochimica et*
833 *Cosmochimica Acta, 268*, 467-484.
834 Christophersen, N., Neal, C., Hooper, R. P., Vogt, R. D., & Andersen, S. (1990).
835 Modelling streamwater chemistry as a mixture of soilwater end-members—a step
836 towards second-generation acidification models. *Journal of Hydrology, 116*(1-4),
837 307-320.
838 Church, P. E., & Granato, G. E. (1996). Bias in ground-water data caused by well-bore
839 flow in long-screen wells. *Groundwater, 34*(2), 262-273.
840 Davis, S. N., & DeWiest, R. J. M. (1966). Hydrogeology John Wiley Sons New York
841 NY.
842 De Simoni, M., Carrera, J., Sanchez-Vila, X., & Guadagnini, A. (2005). A procedure for
843 the solution of multicomponent reactive transport problems. *Water Resources*
844 *Research, 41*(11).
845 Diego-Feliu, M., Rodellas, V., Saaltink, M. W., Alorda-Kleinglass, A., Goyetche, T.,
846 Martínez-Pérez, L., . . . Garcia-Orellana, J. (2021). New perspectives on the use
847 of 224Ra/228Ra and 222Rn/226Ra activity ratios in groundwater studies. *Journal*
848 *of Hydrology, 596*, 126043. doi:10.1016/j.jhydrol.2021.126043
849 Duque, C., Russoniello, C. J., & Rosenberry, D. O. (2020). History and evolution of
850 seepage meters for quantifying flow between groundwater and surface water: Part
851 2–Marine settings and submarine groundwater discharge. *Earth-Science Reviews,*
852 *204*, 103168.
853 Eissa, M. A. (2018). Application of multi-isotopes and geochemical modeling for
854 delineating recharge and salinization sources in Dahab Basin aquifers (South
855 Sinai, Egypt). *Hydrology, 5*(3), 41.
856 Fleury, P., Bakalowicz, M., & de Marsily, G. (2007). Submarine springs and coastal karst
857 aquifers: a review. *Journal of Hydrology, 339*(1-2), 79-92.
858 Folch, A., del Val, L., Luquot, L., Martínez-Pérez, L., Bellmunt, F., Le Lay, H., . . .
859 Carrera, J. (2020). Combining fiber optic DTS, cross-hole ERT and time-lapse
860 induction logging to characterize and monitor a coastal aquifer. *Journal of*
861 *Hydrology, 588*, 125050. doi:10.1016/j.jhydrol.2020.125050
862 Fratesi, B. (2013). Hydrology and geochemistry of the freshwater lens in coastal karst
863 *Coastal karst landforms* (pp. 59-75): Springer.
864 Gattuso, J. P., Frankignoulle, M., Bourge, I., Romaine, S., & Buddemeier, R. W. (1998).
865 Effect of calcium carbonate saturation of seawater on coral calcification. *Global*
866 *and Planetary Change, 18*(1-2), 37-46.
867 Giménez-Forcada, E. (2010). Dynamic of sea water interface using hydrochemical facies
868 evolution diagram. *Groundwater, 48*(2), 212-216.
869 Gomis-Yagües, V., Boluda-Botella, N., & Ruiz-Beviá, F. (2000). Gypsum
870 precipitation/dissolution as an explanation of the decrease of sulphate
871 concentration during seawater intrusion. *Journal of Hydrology, 228*(1-2), 48-55.
872 Grzelak, K., Tamborski, J., Kotwicki, L., & Bokuniewicz, H. (2018). Ecostructuring of
873 marine nematode communities by submarine groundwater discharge. *Marine*
874 *environmental research, 136*, 106-119.

875 Hanshaw, B. B., & Back, W. (1980). Chemical mass-wasting of the northern Yucatan
876 Peninsula by groundwater dissolution. *Geology, 8*(5), 222-224.
877 Hassen, I., Hamzaoui-Azaza, F., & Bouhlila, R. (2018). Establishing complex
878 compartments-aquifers connectivity via geochemical approaches towards
879 hydrogeochemical conceptual model: Kasserine Aquifer System, Central Tunisia.
880 *Journal of Geochemical Exploration, 188*, 257-269.
881 Hooper, R. P. (2003). Diagnostic tools for mixing models of stream water chemistry.
882 *Water Resources Research, 39*(3).
883 Hooper, R. P., Christophersen, N., & Peters, N. E. (1990). Modelling streamwater
884 chemistry as a mixture of soilwater end-members—An application to the Panola
885 Mountain catchment, Georgia, USA. *Journal of Hydrology, 116*(1-4), 321-343.
886 Hurrell, J. W., Holland, M. M., Gent, P. R., Ghan, S., Kay, J. E., Kushner, P. J., . . .
887 Lindsay, K. (2013). The community earth system model: a framework for
888 collaborative research. *Bulletin of the American Meteorological Society, 94*(9),
889 1339-1360.
890 Hutchins, S. R., & Acree, S. D. (2000). Ground water sampling bias observed in shallow,
891 conventional wells. *Groundwater Monitoring & Remediation, 20*(1), 86-93.
892 Jiao, J. J., & Post, V. (2019). *Coastal Hydrogeology*. Cambridge: Cambridge University
893 Press.
894 Jurado, A., Vázquez-Suñé, E., Carrera, J., Tubau, I., & Pujades, E. (2015). Quantifying
895 chemical reactions by using mixing analysis. *Science of The Total Environment,*
896 *502*, 448-456. doi:https://doi.org/10.1016/j.scitotenv.2014.09.036
897 Kendall, C., & Caldwell, E. A. (1998). Chapter 2 - Fundamentals of Isotope
898 Geochemistry. In C. Kendall & J. J. McDonnell (Eds.), *Isotope Tracers in*
899 *Catchment Hydrology* (pp. 51-86). Amsterdam: Elsevier.
900 Kim, J.-H., Kim, K.-H., Thao, N. T., Batsaikhan, B., & Yun, S.-T. (2017). Hydrochemical
901 assessment of freshening saline groundwater using multiple end-members mixing
902 modeling: A study of Red River delta aquifer, Vietnam. *Journal of Hydrology,*
903 *549*, 703-714. doi:https://doi.org/10.1016/j.jhydrol.2017.04.040
904 Kłostowska, Ż., Szymczycha, B., Lengier, M., Zarzeczańska, D., & Dzierzbicka-
905 Głowacka, L. (2020). Hydrogeochemistry and magnitude of SGD in the Bay of
906 Puck, southern Baltic Sea. *Oceanologia, 62*(1), 1-11.
907 doi:10.1016/j.oceano.2019.09.001
908 Kouzana, L., Mammou, A. B., & Felfoul, M. S. (2009). Seawater intrusion and associated
909 processes: Case of the Korba aquifer (Cap-Bon, Tunisia). *Comptes Rendus*
910 *Geoscience, 341*(1), 21-35. doi:10.1016/j.crte.2008.09.008
911 Liu, X., & Millero, F. J. (2002). The solubility of iron in seawater. *Marine Chemistry,*
912 *77*(1), 43-54.
913 Li, P., Wu, J., & Qian, H. (2016). Preliminary assessment of hydraulic connectivity
914 between river water and shallow groundwater and estimation of their transfer rate
915 during dry season in the Shidi River, China. *Environmental Earth Sciences, 75*(2).
916 doi:10.1007/s12665-015-4949-7
917 Liu, Y., Jiao, J. J., Liang, W., & Kuang, X. (2017). Hydrogeochemical characteristics in
918 coastal groundwater mixing zone. *Applied Geochemistry, 85*, 49-60.
919 doi:10.1016/j.apgeochem.2017.09.002
920 Liu, Y., Jiao, J. J., Liang, W., Santos, I. R., Kuang, X., & Robinson, C. E. (2021).
921 Inorganic carbon and alkalinity biogeochemistry and fluxes in an intertidal beach
922 aquifer: Implications for ocean acidification. *Journal of Hydrology, 595*, 126036.
923 doi:https://doi.org/10.1016/j.jhydrol.2021.126036

Long, A. J., & Valder, J. F. (2011). Multivariate analyses with end-member mixing to characterize groundwater flow: Wind Cave and associated aquifers. *Journal of Hydrology, 409*(1), 315-327. doi:10.1016/j.jhydrol.2011.08.028

Luijendijk, E., Gleeson, T., & Moosdorf, N. (2020). Fresh groundwater discharge insignificant for the world's oceans but important for coastal ecosystems. *Nature Communications, 11*(1). doi:10.1038/s41467-020-15064-8

Luo, X., & Jiao, J. J. (2016). Submarine groundwater discharge and nutrient loadings in Tolo Harbor, Hong Kong using multiple geotracer-based models, and their implications of red tide outbreaks. *Water research, 102*, 11-31.

Magaritz, M., Goldenberg, L., Kafri, U., & Arad, A. (1980). Dolomite formation in the seawater–freshwater interface. *Nature, 287*(5783), 622-624.

Mahlknecht, J., Merchán, D., Rosner, M., Meixner, A., & Ledesma-Ruiz, R. (2017). Assessing seawater intrusion in an arid coastal aquifer under high anthropogenic influence using major constituents, Sr and B isotopes in groundwater. *Science of The Total Environment, 587*, 282-295.

Martínez-Pérez, L., Luquot, L., Carrera, J., Marazuela, M. A., Goyetche, T., Pool, M., . . . Folch, A. (2022). A multidisciplinary approach to characterizing coastal alluvial aquifers to improve understanding of seawater intrusion and submarine groundwater discharge. *Journal of Hydrology*, 127510.

Martínez, D., & Bocanegra, E. (2002). Hydrogeochemistry and cation-exchange processes in the coastal aquifer of Mar Del Plata, Argentina. *Hydrogeology Journal, 10*(3), 393-408.

McMahon, P. B., Chapelle, F. H., & Bradley, P. M. (2011). Evolution of redox processes in groundwater *Aquatic Redox Chemistry* (pp. 581-597): ACS Publications.

Milliman, J. D. (1993). Production and accumulation of calcium carbonate in the ocean: Budget of a nonsteady state. *Global Biogeochemical Cycles, 7*(4), 927-957.

Molins, S., Carrera, J., Ayora, C., & Saaltink, M. W. (2004). A formulation for decoupling components in reactive transport problems. *Water Resources Research, 40*(10).

Monastersky, R. (1996). Seep and ye shall find: Hidden water flow. *Science News*, 245-245.

Moore, W. S. (1999). The subterranean estuary: a reaction zone of ground water and sea water. *Marine Chemistry, 65*(1-2), 111-125. doi:10.1016/S0304-4203(99)00014-6

Moore, W. S. (2010). The Effect of Submarine Groundwater Discharge on the Ocean. *Annual Review of Marine Science, 2*(1), 59-88. doi:10.1146/annurev-marine-120308-081019

Morse, J. W., & Berner, R. A. (1995). What determines sedimentary C/S ratios? *Geochimica et Cosmochimica Acta, 59*(6), 1073-1077.

Nakaya, S., Uesugi, K., Motodate, Y., Ohmiya, I., Komiya, H., Masuda, H., & Kusakabe, M. (2007). Spatial separation of groundwater flow paths from a multi-flow system by a simple mixing model using stable isotopes of oxygen and hydrogen as natural tracers. *Water Resources Research, 43*(9).

Palacios, A., Ledo, J. J., Linde, N., Luquot, L., Bellmunt, F., Folch, A., . . . Martínez, L. (2020). Time-lapse cross-hole electrical resistivity tomography (CHERT) for monitoring seawater intrusion dynamics in a Mediterranean aquifer. *Hydrology and Earth System Sciences, 24*(4), 2121-2139.

Pelizardi, F., Bea, S. A., Carrera, J., & Vives, L. (2017). Identifying geochemical processes using End Member Mixing Analysis to decouple chemical components for mixing ratio calculations. *Journal of Hydrology, 550*, 144-156.

973 Peng, T., Zhu, Z., Du, J., & Liu, J. (2021). Effects of nutrient-rich submarine groundwater
974 discharge on marine aquaculture: A case in Lianjiang, East China Sea. *Science of*
975 *The Total Environment*, 147388.
976 Poulsen, D. L., Cook, P. G., Simmons, C. T., McCallum, J. L., & Dogramaci, S. (2019).
977 Effects of intraborehole flow on purging and sampling long-screened or open
978 wells. *Groundwater*, *57*(2), 269-278.
979 Pulido-Leboeuf, P. (2004). Seawater intrusion and associated processes in a small coastal
980 complex aquifer (Castell de Ferro, Spain). *Applied Geochemistry, 19*(10), 1517-
981 1527.
982 Rezaei, M., Sanz, E., Raeisi, E., Ayora, C., Vázquez-Suñé, E., & Carrera, J. (2005).
983 Reactive transport modeling of calcite dissolution in the fresh-salt water mixing
984 zone. *Journal of Hydrology*, *311*(1-4), 282-298.
985 Rosecrans, C. Z., Nolan, B. T., & Gronberg, J. M. (2017). Prediction and visualization of
986 redox conditions in the groundwater of Central Valley, California. *Journal of*
987 *Hydrology*, *546*, 341-356.
988 Rufí-Salís, M., Garcia-Orellana, J., Cantero, G., Castillo, J., Hierro, A., Rieradevall, J., &
989 Bach, J. (2019). Influence of land use changes on submarine groundwater
990 discharge. *Environmental Research Communications*, *1*(3), 031005.
991 doi:10.1088/2515-7620/ab1695
992 Russak, A., & Sivan, O. (2010). Hydrogeochemical Tool to Identify Salinization or
993 Freshening of Coastal Aquifers Determined from Combined Field Work,
994 Experiments, and Modeling. *Environmental Science & Technology*, *44*(11), 4096-
995 4102. doi:10.1021/es1003439
996 Russak, A., Sivan, O., & Yechieli, Y. (2016). Trace elements (Li, B, Mn and Ba) as
997 sensitive indicators for salinization and freshening events in coastal aquifers.
998 *Chemical Geology*, *441*, 35-46.
999 Rusydi, A. F., Onodera, S.-I., Saito, M., Ioka, S., Maria, R., Ridwansyah, I., & Delinom,
1000 R. M. (2021). Vulnerability of groundwater to iron and manganese contamination
1001 in the coastal alluvial plain of a developing Indonesian city. *SN Applied Sciences*,
1002 *3*(4), 1-12.
1003 Santos, I. R. S., Burnett, W. C., Chanton, J., Mwashote, B., Suryaputra, I. G. N. A., &
1004 Dittmar, T. (2008). Nutrient biogeochemistry in a Gulf of Mexico subterranean
1005 estuary and groundwater-derived fluxes to the coastal ocean. *Limnology and*
1006 *Oceanography*, *53*(2), 705-718. doi:https://doi.org/10.4319/lo.2008.53.2.0705
1007 Sawyer, A. H., Michael, H. A., & Schroth, A. W. (2016). From soil to sea: the role of
1008 groundwater in coastal critical zone processes. *WIREs Water*, *3*(5), 706-726.
1009 doi:https://doi.org/10.1002/wat2.1157
1010 Scott, G., & Crunkilton, R. L. (2000). Acute and chronic toxicity of nitrate to fathead
1011 minnows (Pimephales promelas), ceriodaphnia dubia, and Daphnia magna.
1012 *Environmental Toxicology and Chemistry*, *19*(12), 2918-2922.
1013 doi:https://doi.org/10.1002/etc.5620191211
1014 Shalev, E., Lazar, A., Wollman, S., Kington, S., Yechieli, Y., & Gvirtzman, H. (2009).
1015 Biased Monitoring of Fresh Water-Salt Water Mixing Zone in Coastal Aquifers.
1016 *Groundwater*, *47*(1), 49-56. doi:https://doi.org/10.1111/j.1745-
1017 6584.2008.00502.x
1018 Shin, K., Koh, D.-C., Jung, H., & Lee, J. (2020). The Hydrogeochemical Characteristics
1019 of Groundwater Subjected to Seawater Intrusion in the Archipelago, Korea.
1020 *Water*, *12*(6), 1542.
1021 Sivan, O., Yechieli, Y., Herut, B., & Lazar, B. (2005). Geochemical evolution and
1022 timescale of seawater intrusion into the coastal aquifer of Israel. *Geochimica et*

Cosmochimica Acta, *69*(3), 579-592. doi:https://doi.org/10.1016/j.gca.2004.07.023

Slomp, C. P., & Van Cappellen, P. (2004). Nutrient inputs to the coastal ocean through submarine groundwater discharge: controls and potential impact. *Journal of Hydrology*, *295*(1), 64-86. doi:10.1016/j.jhydrol.2004.02.018

Small, C., & Nicholls, R. J. (2003). A global analysis of human settlement in coastal zones. *Journal of Coastal Research*, 584-599.

Snyder, M., Taillefert, M., & Ruppel, C. (2004). Redox zonation at the saline-influenced boundaries of a permeable surficial aquifer: effects of physical forcing on the biogeochemical cycling of iron and manganese. *Journal of Hydrology*, *296*(1), 164-178. doi:10.1016/j.jhydrol.2004.03.019

Spotte, S. (1979). Fish and invertebrate culture: water management in closed systems-2.

Sutcliffe Jr, W. H. (1972). Some relations of land drainage, nutrients, particulate material, and fish catch in two eastern Canadian bays. *Journal of the Fisheries Board of Canada*, *29*(4), 357-362.

Taniguchi, M., Dulai, H., Burnett, K. M., Santos, I. R., Sugimoto, R., Stieglitz, T., . . . Burnett, W. C. (2019). Submarine groundwater discharge: updates on its measurement techniques, geophysical drivers, magnitudes, and effects. *Frontiers in Environmental Science*, *7*, 141.

Tubau, I., Vàzquez-Suñé, E., Jurado, A., & Carrera, J. (2014). Using EMMA and MIX analysis to assess mixing ratios and to identify hydrochemical reactions in groundwater. *Science of The Total Environment, 470-471*, 1120-1131. doi:10.1016/j.scitotenv.2013.10.121

U. S. Environmental Protection Agency. (1986). *Quality criteria for water* (EPA 440/5-86-0013). Retrieved from Washington, DC.:

Valiela, I., Costa, J., Foreman, K., Teal, J. M., Howes, B., & Aubrey, D. (1990). Transport of groundwater-borne nutrients from watersheds and their effects on coastal waters. *Biogeochemistry*, *10*(3), 177-197. doi:10.1007/BF00003143

van Hulten, M., Dutay, J. C., Middag, R., de Baar, H., Roy-Barman, M., Gehlen, M., Tagliabue, A. & Sterl, A. (2016). Manganese in the world ocean: A first global model. *Biogeosciences Discuss*, *14*, 1-38.

Velasco, J., Lloret, J., Millán, A., Marin, A., Barahona, J., Abellán, P., & Sánchez-Fernández, D. (2006). Nutrient and particulate inputs into the Mar Menor lagoon (SE Spain) from an intensive agricultural watershed. *Water, Air, and Soil Pollution*, *176*(1), 37-56.

Vázquez-Suñé, E., Carrera, J., Tubau, I., Sánchez-Vila, X., & Soler, A. (2010). An approach to identify urban groundwater recharge. *Hydrology and Earth System Sciences*, *14*(10), 2085-2097. doi:10.5194/hess-14-2085-2010

Wicks, C. M., & Herman, J. S. (1996). Regional hydrogeochemistry of a modern coastal mixing zone. *Water Resources Research*, *32*(2), 401-407.

Wigley, T. M. L., & Plummer, L. N. (1976). Mixing of carbonate waters. *Geochimica et Cosmochimica Acta*, *40*(9), 989-995. doi:10.1016/0016-7037(76)90041-7

Wilkinson, B. H., & Algeo, T. J. (1989). Sedimentary carbonate record of calcium-magnesium cycling. *American Journal of Science*, *289*(10), 1158-1194.

Windom, H. L., Moore, W. S., Niencheski, L. F. H., & Jahnke, R. A. (2006). Submarine groundwater discharge: A large, previously unrecognized source of dissolved iron to the South Atlantic Ocean. *Marine Chemistry*, *102*(3), 252-266. doi:10.1016/j.marchem.2006.06.016